

<https://doi.org/10.14379/iodp.proc.372B375.101.2019>



## Expedition 372B/375 summary<sup>1</sup>

D.M. Saffer, L.M. Wallace, P.M. Barnes, I.A. Pecher, K.E. Petronotis, L.J. LeVay, R.E. Bell, M.P. Crundwell, C.H. Engelmann de Oliveira, A. Fagereng, P.M. Fulton, A. Greve, R.N. Harris, Y. Hashimoto, A. Hüpers, M.J. Ikari, Y. Ito, H. Kitajima, S. Kutterolf, H. Lee, X. Li, M. Luo, P.R. Malie, F. Meneghini, J.K. Morgan, A. Noda, H.S. Rabinowitz, H.M. Savage, C.L. Shepherd, S. Shreedharan, E.A. Solomon, M.B. Underwood, M. Wang, A.D. Woodhouse, S.M. Bourlange, M.M.Y. Brunet, S. Cardona, M.B. Clennell, A.E. Cook, B. Dugan, J. Elger, D. Gamboa, A. Georgiopoulou, S. Han, K.U. Heeschen, G. Hu, G.Y. Kim, H. Koge, K.S. Machado, D.D. McNamara, G.F. Moore, J.J. Mountjoy, M.A. Nole, S. Owari, M. Paganoni, P.S. Rose, E.J. Screaton, U. Shankar, M.E. Torres, X. Wang, and H.-Y. Wu<sup>2</sup>

**Keywords:** International Ocean Discovery Program, IODP, *JOIDES Resolution*, Expedition 372, Expedition 375, Site U1518, Site U1519, Site U1520, Site U1526, Hikurangi margin, slow slip events, observatories, subduction

### Abstract

Slow slip events (SSEs) at the northern Hikurangi subduction margin, New Zealand, are among the best-documented shallow SSEs on Earth. International Ocean Discovery Program Expeditions 372 and 375 were undertaken to investigate the processes and in situ conditions that underlie subduction zone SSEs at the northern Hikurangi Trough. We accomplished this goal by (1) coring and geophysical logging at four sites, including penetration of an active thrust fault (the Pāpaku fault) near the deformation front, the upper plate above the SSE source region, and the incoming sedimentary succession in the Hikurangi Trough and atop the Tūranganui Knoll seamount; and (2) installing borehole observatories in the Pāpaku fault and in the upper plate overlying the slow slip source region. Logging-while-drilling (LWD) data for this project were acquired as part of Expedition 372, and coring, wireline logging, and observatory installations were conducted during Expedition 375.

Northern Hikurangi subduction margin SSEs recur every 1–2 y and thus provide an ideal opportunity to monitor deformation and associated changes in chemical and physical properties throughout the slow slip cycle. In situ measurements and sampling of material from the sedimentary section and oceanic basement of the sub-

ducting plate reveal the rock properties, composition, lithology, and structural character of material that is transported downdip into the SSE source region. A recent seafloor geodetic experiment raises the possibility that SSEs at northern Hikurangi may propagate to the trench, indicating that the shallow thrust fault (the Pāpaku fault) targeted during Expeditions 372 and 375 may also lie in the SSE rupture area and host a portion of the slip in these events. Hence, sampling and logging at this location provides insights into the composition, physical properties, and architecture of a shallow fault that may host slow slip.

Expeditions 372 and 375 were designed to address three fundamental scientific objectives:

1. Characterize the state and composition of the incoming plate and shallow fault near the trench, which comprise the protolith and initial conditions for fault zone rock at greater depth and which may itself host shallow slow slip;
2. Characterize material properties, thermal regime, and stress conditions in the upper plate directly above the SSE source region; and
3. Install observatories in the Pāpaku fault near the deformation front and in the upper plate above the SSE source to measure

<sup>1</sup> Saffer, D.M., Wallace, L.M., Barnes, P.M., Pecher, I.A., Petronotis, K.E., LeVay, L.J., Bell, R.E., Crundwell, M.P., Engelmann de Oliveira, C.H., Fagereng, A., Fulton, P.M., Greve, A., Harris, R.N., Hashimoto, Y., Hüpers, A., Ikari, M.J., Ito, Y., Kitajima, H., Kutterolf, S., Lee, H., Li, X., Luo, M., Malie, P.R., Meneghini, F., Morgan, J.K., Noda, A., Rabinowitz, H.S., Savage, H.M., Shepherd, C.L., Shreedharan, S., Solomon, E.A., Underwood, M.B., Wang, M., Woodhouse, A.D., Bourlange, S.M., Brunet, M.M.Y., Cardona, S., Clennell, M.B., Cook, A.E., Dugan, B., Elger, J., Gamboa, D., Georgiopoulou, A., Han, S., Heeschen, K.U., Hu, G., Kim, G.Y., Koge, H., Machado, K.S., McNamara, D.D., Moore, G.F., Mountjoy, J.J., Nole, M.A., Owari, S., Paganoni, M., Rose, P.S., Screaton, E.J., Shankar, U., Torres, M.E., Wang, X., and Wu, H.-Y., 2019. Expedition 372B/375 summary. In Wallace, L.M., Saffer, D.M., Barnes, P.M., Pecher, I.A., Petronotis, K.E., LeVay, L.J., and the Expedition 372/375 Scientists, *Hikurangi Subduction Margin Coring, Logging, and Observatories*. Proceedings of the International Ocean Discovery Program, 372B/375: College Station, TX (International Ocean Discovery Program). <https://doi.org/10.14379/iodp.proc.372B375.101.2019>

<sup>2</sup> Expedition 372B/375 Scientists' affiliations.

MS 372B375-101: Published 5 May 2019

This work is distributed under the [Creative Commons Attribution 4.0 International](https://creativecommons.org/licenses/by/4.0/) (CC BY 4.0) license. 

### Contents

- 1 Abstract
- 2 Introduction
- 3 Background
- 4 Scientific objectives (overall primary and secondary objectives)
- 7 Site summaries
- 29 Observatory installations
- 29 Preliminary scientific assessment
- 32 References

temporal variations in deformation, temperature, and fluid flow. The observatories will monitor volumetric strain (via pore pressure as a proxy) and the evolution of physical, hydrological, and chemical properties throughout the SSE cycle.

Together, the coring, logging, and observatory data will test a suite of hypotheses about the fundamental mechanics and behavior of SSEs and their relationship to great earthquakes along the subduction interface.

## Introduction

Slow slip events (SSEs) involve transient aseismic slip on a fault (lasting weeks to years) at a slip velocity intermediate between plate tectonic rates and those required to radiate seismic waves. Only since the advent of dense, plate boundary–scale geodetic networks in the last ~15 y has the importance of these events as a significant mode of fault slip been recognized. The observation of SSEs and associated seismic phenomena (e.g., tremor and low-frequency earthquakes) along subduction megathrusts worldwide (e.g., Schwartz and Rokosky, 2007) has ignited one of the most dynamic fields of current research in seismology (e.g., Rubinstein et al., 2010; Peng and Gomberg, 2010; Wech and Creager, 2011). Despite this intense interest, the physical mechanisms that underlie SSEs and the rela-

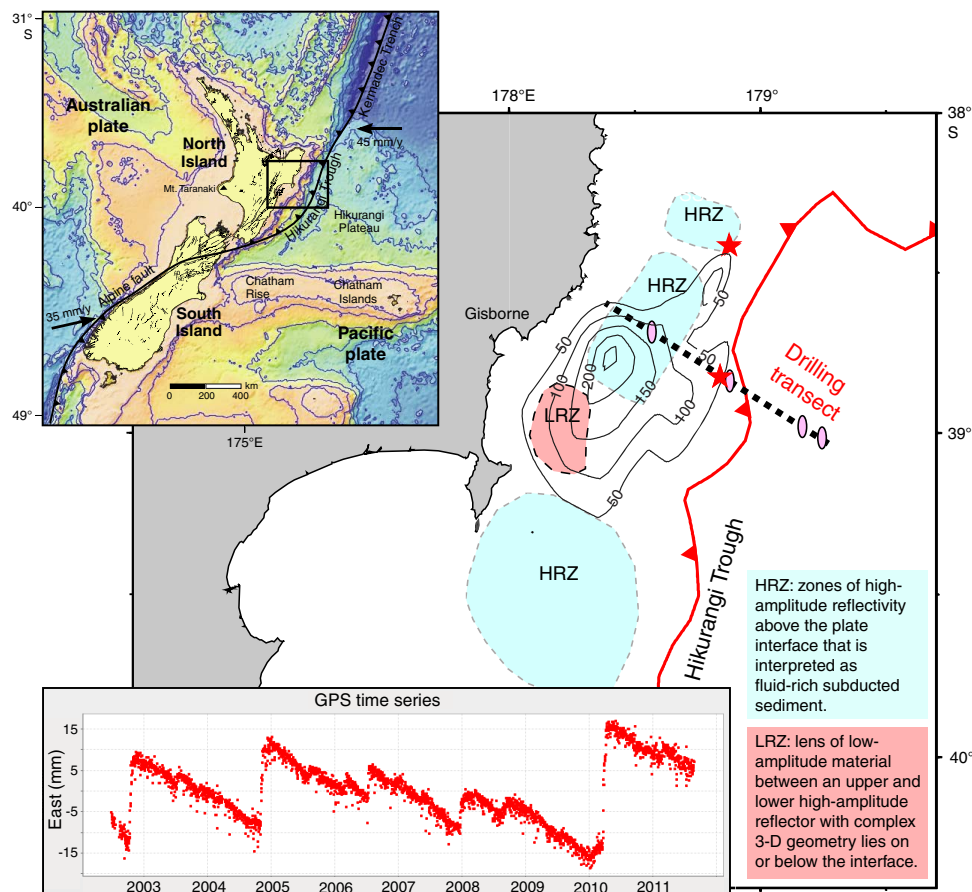
tionship of SSEs to destructive seismic slip on subduction thrusts are poorly known.

This deficiency in our understanding of SSEs is partly due to the fact that most well-studied subduction zone SSEs (e.g., Cascadia and southwest Japan) occur too deep for high-resolution imaging or direct sampling of the source region. A notable exception is the northern Hikurangi margin, New Zealand, where well-characterized SSEs occur every 1–2 y over a period of 2–3 weeks at depths <2–15 km below the seafloor (Wallace and Beavan, 2010; Wallace et al., 2016) (Figure F1). The proximity of SSEs to the seafloor makes it feasible to drill into and sample, collect downhole logs from, and conduct monitoring in the near field of the SSEs and potentially even in the faults that host these events. The regularity and well-characterized short repeat interval of the SSEs allow monitoring over multiple SSE cycles, with the potential to document the spatial and temporal distribution of strain accumulation and release and any associated hydrogeologic phenomena.

The scientific objectives of International Ocean Discovery Program (IODP) Expeditions 372 and 375 were threefold:

- Document the physical properties, hydrogeological properties, chemical properties, lithology, geometry, microstructure, and thermal state of the subduction inputs and Pāpaku fault located near (and possibly in) the shallowest reaches of SSE slip. The in-

Figure F1. Tectonic setting (upper left inset) and location of slip on the interface in September/October 2014 captured by a seafloor network of Absolute Pressure Gauges (black contours, labeled in 50 mm increments; Wallace et al., 2016) and the reflective properties of the subduction interface (Bell et al., 2010) at northern Hikurangi. Black dashed line = location of the drilling transect (see Figure F2), pink ellipses = drill sites, stars = locations of two tsunamigenic subduction interface earthquakes (Mw 6.9–7.1) in March and May of 1947. LRZ = low reflectivity zone, HRZ = high reflectivity zone. Lower left inset: east component of the position-time series for a cGPS site near Gisborne that demonstrates the repeatability of SSEs since they were first observed in 2002.



puts include the sediment and upper igneous crust of the subducting Pacific plate, with an emphasis on intervals that host or will eventually host SSEs.

- Define the stress regime, thermal structure, porosity, permeability, lithology, pore fluid pressure state, fluid chemistry, flow pathways, and structural geology of the upper plate overlying the SSE source region.
- Install observatories in the upper plate and in the Pāpaku fault that together span the SSE source region to monitor deformation and changes in temperature and hydrogeology related to SSEs.

## Background

### Geological setting

In the region of the Expedition 372 and 375 drilling transect, the Pacific plate subducts westward beneath the North Island of New Zealand along the Hikurangi Trough at 4.5–5.5 cm/y (Wallace et al., 2004) (Figure F1). The subducting plate is composed of the Hikurangi Plateau, a Cretaceous large igneous province. The plateau sequence is overlain by a ~1 km thick Cenozoic to Mesozoic sedimentary sequence (Figure F2) that increases to >5 km in thickness to the south (e.g., south of ~40°S). The northern part of the margin is currently primarily nonaccretionary and locally exhibits frontal tectonic erosion associated with subducting seamounts (Lewis et al., 1998; Collot et al., 2001; Pedley et al., 2010). Where accretion does occur, the margin is characterized by a narrow, steeply tapered (>10° taper angle) wedge (Barker et al., 2009). A number of seamounts are present on the Pacific plate approaching the deformation front (e.g., Tūranganui Knoll and Puke seamounts). The subduction thrust is identified as a décollement between a highly deformed imbricated thrust wedge above a relatively less deformed subducting sequence.

SSEs at the northern Hikurangi margin occur every 18–24 months and typically involve 1–3 cm of southeastward surface displacement at continuously operating GPS (cGPS) sites (Figure F1) along the coast. The portion of the subduction interface that undergoes slow slip is almost fully locked between the SSEs, and this slip deficit is mostly or completely recovered by the SSEs (Wallace and Beavan, 2010). The equivalent moment magnitudes of the largest SSEs are typically Mw 6.5–7.0, with average slip of ~7–20 cm on the plate interface. These larger SSEs are punctuated by more frequent smaller events (one or more per year) that are not as well character-

ized (see GPS time series inset in Figure F1). SSE slip in this area is predominantly offshore, and the events appear to repeatedly rupture similar areas of the interface (Wallace and Beavan, 2010). A recent seafloor geodetic experiment has shown that slow slip occurs to within  $\leq 2$  km of the seafloor along the Expedition 375 drilling transect, and it is possible that slow slip continues all the way to the trench (Wallace et al., 2016).

Multichannel seismic data reveal that the source areas of some SSEs (between <5 and >10–16 km depth) correspond to the top of a thick high reflectivity zone (HRZ) (Figures F1, F2) (Bell et al., 2010). The high-amplitude reflectivity has been hypothesized to result from undercompaction and high fluid pressures in sediments entrained between downgoing seamounts. Alternatively, the reflectors may represent lithologic packages (e.g., altered basaltic lavas or volcanoclastic sediments). If the former interpretation is correct, then the inferred correlation between the HRZ and SSEs would support the idea that fluid pressure is associated with the generation of slow slip by reducing effective stress; if the latter interpretation is correct, the correlation would suggest a compositional control on fault slip behavior (e.g., Kodaira et al., 2004; Liu and Rice, 2007; Audet et al., 2009; Song et al., 2009; Saffer and Wallace, 2015).

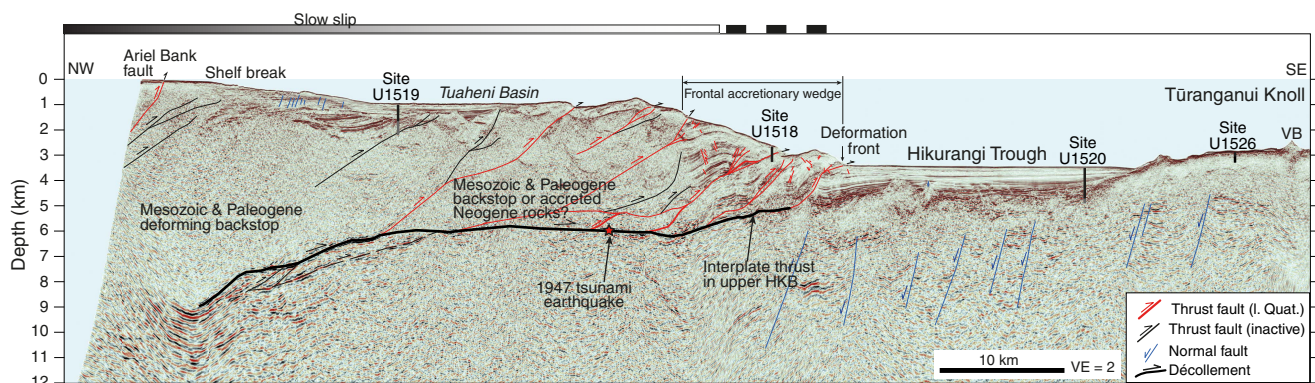
### Previous drilling in the region

No previous scientific drilling has been undertaken at the Hikurangi subduction margin. A total of 44 industry exploration wells have been drilled onshore, ranging in depth from <100 to 4352 m, and 3 have been drilled offshore the east coast of the North Island. These wells target the East Coast Basin, which overlies much of the inner Hikurangi forearc.

Previous drilling during Ocean Drilling Program Leg 181 targeted the eastern portion of the Hikurangi Plateau (Sites 1123 and 1124) ~900 and ~600 km, respectively, east of the coast of the North Island (Davy et al., 2008). Results of this drilling allow a preliminary correlation of seismic facies (Plaza-Faverola et al., 2012; Ghisetti et al., 2016; Barnes et al., 2018) that suggests the following Hikurangi Plateau stratigraphy:

- A basal sequence of high-velocity (>4 km/s) basaltic rocks;
- An overlying 3 km thick Hikurangi Basement Sequence (HKB) interpreted to comprise 120 Ma volcanoclastics and/or chert or limestone;
- A late-stage (100–90 Ma) volcanic cone and seamount constructional sequence;

Figure F2. Depth-converted Seismic Profile 05CM-04 showing locations and depths of sites drilled during Expedition 375 and structural interpretation (modified from Barker et al., 2018). Star = projected location of March 1947 tsunami earthquake. Location of the profile coincides with the drilling transect shown in Figure F1. VB = volcanic cone. VE = vertical exaggeration.



- A 150–230 m thick sedimentary cover sequence comprising an upper sequence (70–32 Ma) of nannofossil chalk and mudstone and a possible lower sequence (100–70 Ma) of clastic sedimentary rocks; and
- A 1000–1200 m thick trench-fill cover sequence of late Cenozoic turbidites, mudstone, and debris flow deposits. At the deformation front beneath Puke Ridge (Figure F2), the subduction décollement lies ~2 km below the seabed in the upper part of the HKB.

## Scientific objectives (overall primary and secondary objectives)

Logging (including LWD and wireline logging), coring, and long-term observatories installed at the Hikurangi subduction margin drill sites during Expeditions 372 and 375 were planned to address a suite of hypotheses regarding slow slip and the mechanics of subduction megathrusts:

- SSEs propagate to the trench. They are not confined to a specific (narrow) pressure or temperature range.
- Pore fluid pressure is elevated in the source region of SSEs. The elevated pore pressures are driven by a combination of compaction disequilibrium and mineral dehydration reactions that occur as sediments and altered igneous crust on the incoming plate are buried and heated during subduction.
- SSEs occur in regions of conditional frictional stability. A single fault patch can exhibit different slip modes (e.g., steady creep, episodic slow slip, or seismic slip) depending on in situ conditions and state.
- A continuum of duration and magnitude characteristics of SSEs and slow seismic behavior occurs along the shallowest reaches of the subduction megathrust.
- SSEs drive fluid flow and chemical transport along faults and throughout the upper plate.

Expeditions 372 and 375 undertook a coordinated program of LWD, coring, and observatory installation framed around three pri-

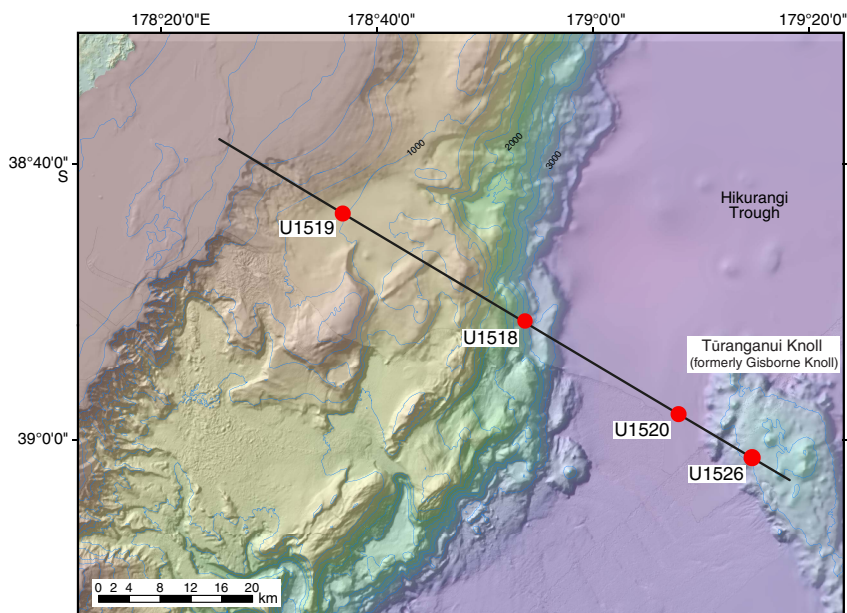
mary scientific objectives designed to test these hypotheses. These scientific objectives are outlined here and addressed in further detail below.

1. *Characterize the compositional, thermal, hydrogeological, frictional, geochemical, structural, and diagenetic conditions of the subducting material and Pāpaku fault.*

Achieving this objective requires characterization of the incoming stratigraphy and upper oceanic basement rocks, together with the Pāpaku fault, which forms a shallow active strand of the frontal thrust system. This characterization involves a combination of coring, downhole measurements, and logging at originally proposed Sites HSM-05A (now Site U1520; sedimentary succession on subducting plate), HSM-08A (now Site U1526; seamount on subducting plate), and HSM-15A (now Site U1518; Pāpaku fault) (Figure F3), followed by a strategy of coordinated post-expedition laboratory analyses (Saffer et al., 2017). Site U1518 provides material from an active thrust in the updip region of the plate interface early in its evolution, at low temperature and low effective stress. If SSEs propagate onto splay faults near the deformation front, the Pāpaku fault zone sampled at Site U1518 may undergo slow slip; this possibility will be tested using data from the observatory installed during the expedition. Site U1520 targeted the sediment package on top of the Hikurangi Plateau. Site U1526 targeted a representative section of the upper portion of the Tūrangānuī Knoll seamount, which was thought to be composed of volcanoclastic sediment or altered basaltic basement.

LWD data acquired during Expedition 372 at Sites U1518 and U1520 documented sediment properties and structure and characterized stress orientations through analysis of wellbore failures at Site U1518 (see the [Site U1518](#) and [Site U1520](#) chapters [Saffer et al., 2019; Barnes et al., 2019c]). Coring during Expedition 375 aimed to collect key samples and data sets for sediment/rock physical properties, pore fluid composition, and downhole temperature with a focus on hydrogeology and fault mechanical processes. Together, these data define the initial conditions and composition for both the subducting crust and interstitial pore fluids, and samples of the in-

Figure F3. Bathymetry and locations of Seismic Line 05CM-04 (black line) (see Figure F2) and Expedition 375 sites.



coming materials will be used for laboratory experimental studies of rock physical and chemical properties to understand the in situ properties and their evolution with progressive subduction. These data and post-expedition studies will also yield critical information to refine depth conversion of existing 2-D and 3-D seismic data and thus to quantitatively extend knowledge of in situ properties and conditions (stress, fault zone properties, and pore pressure) from the boreholes to a broader region (e.g., Tobin and Saffer, 2009). Ultimately, samples and geophysical data acquired at Sites U1518, U1520, and U1526 will constrain (1) the composition and frictional properties of subduction inputs and the shallow plate interface, (2) the hydrologic and thermal conditions of the incoming plate and shallow fault, and (3) the structural character, stress conditions, and mechanical properties of the main active thrust and subduction inputs.

Downhole temperature measurements were planned to define temperature profiles and, in combination with measurements of thermal properties on core samples, provide information about shallow heat flow across the margin. These data will be used to constrain thermal models of the margin that define margin temperature structure and thus the thermal, diagenetic, and metamorphic environment of SSEs and to identify potential advective signatures associated with active fluid flow (e.g., Saffer et al., 2008; Peacock, 2009; Saffer and Wallace, 2015).

### 2. Characterize the properties and conditions in the upper plate overlying the SSE source region.

LWD resistivity image data acquired during Expedition 372 at Site U1519 provide key information about fracture and faulting patterns. The data also document borehole breakouts, providing information about the maximum and minimum horizontal stress orientations. In combination with rock physical properties data acquired from cores during Expedition 375, these data may also be used to estimate horizontal stress magnitudes (e.g., Moos and Zoback, 1990; Zoback et al., 2007; Chang et al., 2010; Lin et al., 2013; Huffman and Saffer, 2016).

Core samples from Site U1519 acquired during Expedition 375 will also enable measurements of rock elastic and other physical properties needed to confidently interpret observatory data (e.g., Wang and Davis, 1996; Sawyer et al., 2008; Hammerschmidt et al., 2013), to assess the role of upper plate properties in possible triggering of SSEs (e.g., Wallace et al., 2017), and to define realistic rock properties to inform models of SSE slip (e.g., Williams and Wallace, 2018). Analysis of pore fluid chemistry allows identification of the

source region of fluids in the hanging wall above and surrounding the SSE region to assess whether fluids from depth flow upward and escape through the fractured and structurally disrupted hanging wall and to quantify flow pathways, rates, and driving forces (e.g., Kopf et al., 2003; Hensen et al., 2004; Ranero et al., 2008; Kastner et al., 2014).

### 3. Monitor deformation, hydrogeology, and chemistry via borehole observatories.

Installation of borehole observatories was planned in the Pāpaku fault (Site U1518) and in the hanging wall above the source area of large SSE slip (Site U1519) (Figures F2, F3). The observatory at Site U1518 includes multilevel pore fluid pressure sensing above, in, and below the fault zone and high-resolution downhole temperature monitoring using a string of 30 autonomous temperature sensors (Figures F4, F5). Time series of fluid flow rates and fluid geochemistry in the fault zone interval will be collected using OsmoSamplers and an OsmoFlowmeter (Jannasch et al., 2004; Solomon et al., 2009). The observatory at Site U1519 involves a simpler design (Figure F4) with two levels of formation pressure sensing and a string of 15 temperature sensors. Both observatories incorporate pressure sensing at the wellhead to provide a seafloor reference for the downhole pressure sensors to allow removal of oceanographic signals; the wellhead sensors may also provide data to resolve vertical deformation of the seafloor (e.g., Wallace et al., 2016).

The main goals of the observatories are as follows:

- Monitor temporal variations in pore fluid pressure, temperature, fluid geochemistry, and flow rate in the fault zone, hanging wall, and footwall of the Pāpaku fault (Site U1518) as well as pressure and temperature in the hanging wall further landward (Site U1519) through several SSE cycles. These data will quantify ambient pore pressure, provide information about potential links between hydraulic and geochemical transients and SSEs, and constrain the source region of fluids associated with SSEs (e.g., Solomon et al., 2009; Davis et al., 2011).
- Determine ambient temperatures and the geothermal gradient to better constrain the thermal regime of slow slip.
- Determine formation hydraulic and elastic properties using tidal and other oceanographic forcings (e.g., Kinoshita et al., 2018).
- Integrate pore pressure changes (as a direct proxy for volumetric strain) in a broader framework of deformation monitoring from an existing network of onshore cGPS and seafloor sensors to constrain the spatial and temporal distribution of slip during SSEs (e.g., Araki et al., 2017).

Figure F4. Observatory configurations, Sites U1518 and U1519.

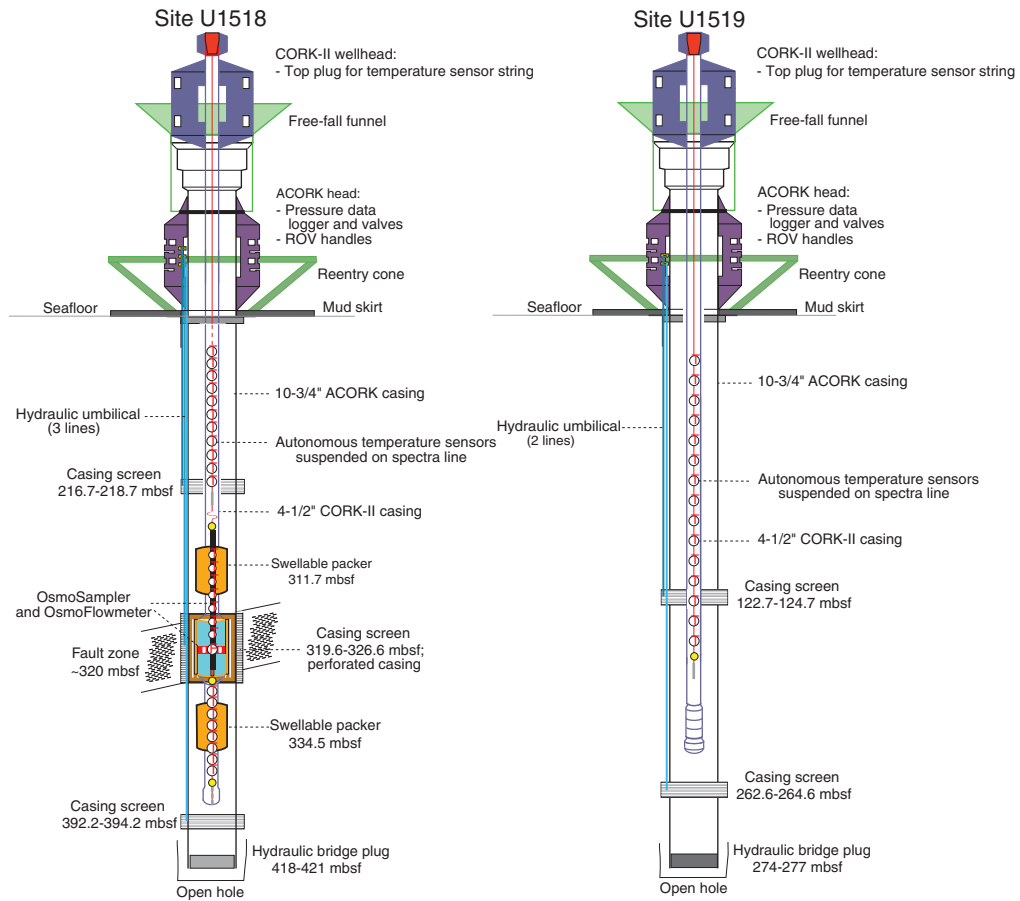
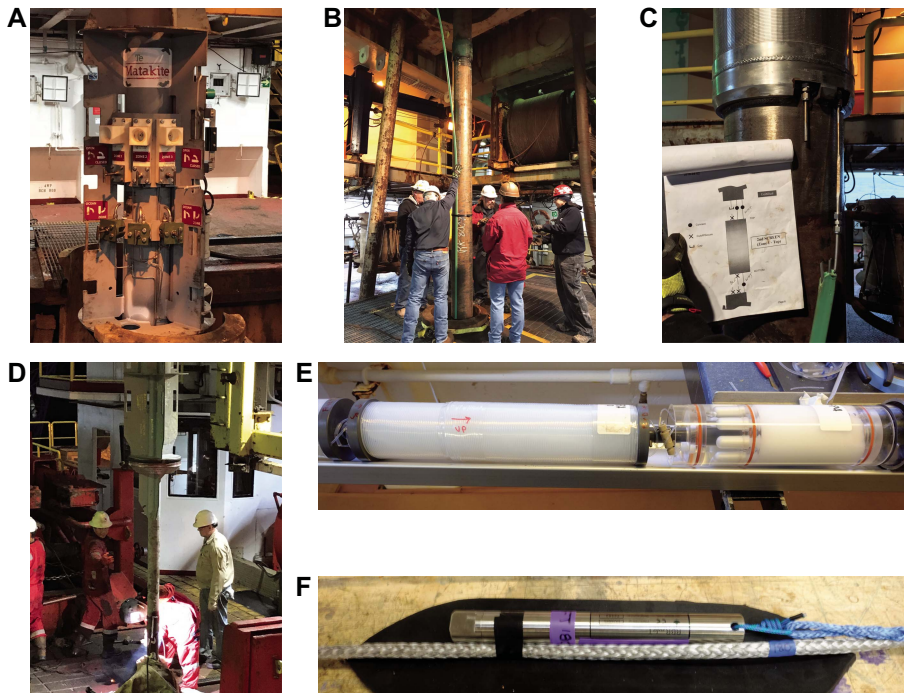


Figure F5. Observatory components of ACORK and CORK-II installations. A. ACORK wellhead with bay containing valves facing forward, Hole U1518H. B. Attachment of hydraulic umbilical to ACORK casing in the moonpool, Hole U1518H. C. Hydraulic line connections at the base of an ACORK casing screen, Hole U1519B. D. CORK-II wellhead connection to 4½ inch casing at the rig floor, Hole U1519B. E. OsmoSampler pump (right) and Teflon coil (left), Hole U1518H. F. Miniature temperature sensor attached to Spectra line prior to wrapping and taping, Hole U1518H.



## Site summaries

### Site U1518

#### Background and objectives

Site U1518 is located on the lower continental slope near the trench and ~73 km from shore at ~2630 m water depth (Figures F2, F3; Table T1) (see the [Site U1518](#) chapter [Saffer et al., 2019]). This site is located on the forelimb of an anticline formed by an active thrust, the Pāpaku fault, which branches from the plate interface (Figure F2). The fault is thought to accommodate a component of plate motion in this portion of the Hikurangi margin, and it is possible that it hosts SSEs. Both LWD during Expedition 372 and coring during Expedition 375 were planned to extend through the Pāpaku fault near the deformation front, terminating 150–200 m into the footwall (Figure F2). Drilling was expected to encounter accreted Pleistocene trench-fill sediments comprising hemipelagic mud, sand and mud turbidites, ash, and mass transport deposits (MTDs) in both the hanging wall and footwall. The primary operational objectives at this site were (1) coring and downhole logging to total depth with the highest priority of sampling the lower ~100 m of the hanging wall, the fault zone, and the footwall of the thrust (including additional possible deeper subsidiary faults suggested on the basis of seismic data) and (2) installing a subseafloor observatory to monitor changes throughout the slow slip cycle in and surrounding the fault zone.

The main scientific objectives of coring and downhole logging at Site U1518 were to define the structures and deformation, physical properties, lithology and composition, and interstitial fluid geochemistry of the active thrust fault and surrounding sediments. Coring and LWD results were used to define the depth interval for observatory pore pressure monitoring and geochemical sampling in the fault zone and to select optimal locations for pore pressure monitoring in the hanging wall and footwall.

Key foci for post-expedition studies on core samples and downhole logging data include but are not limited to

- Structural analyses to characterize deformation mechanisms and style and fracture and fault orientations (e.g., Byrne et al., 2009);
- Analysis of wellbore failures (breakouts and tensile fractures) to characterize contemporary maximum and minimum stress orientations and, with constraints on rock strength, potentially constrain absolute stress magnitudes;
- Laboratory measurements of fault and wall rock rheology to test hypotheses linking fault constitutive properties to slip behavior (e.g., Saffer and Wallace, 2015; Leeman et al., 2016);
- Geomechanical and thermal properties measurements to define poroelastic, strength, and heat transport properties of the formation and to guide interpretation of observatory data (e.g., Wang, 2004; Sawyer et al., 2008; Davis et al., 2009; Kinoshita et al., 2018); and
- Strength, permeability, and elastic moduli measurements to provide context for the interpretation of borehole failures as indicators of in situ stress magnitude, parameterization of deformation and hydrologic models, and core-log-seismic integration.

#### Expedition 372 operations

##### Transit to Site U1518

The ship arrived at Site U1518 (proposed Site HSM-15A [Saffer et al., 2017]) at 1635 h (UTC + 13 h) on 19 December 2017 after a 20 nmi transit from Site U1517.

##### Hole U1518A

Hole U1518A (38°51.5368'S, 178°53.7606'E; 2636.4 meters below sea level [mbsl]) was spudded at 0855 h on 20 December 2017 and 24 h safety monitoring began. The LWD bottom-hole assembly (BHA) contained the geoVISION, NeoScope, StethoScope, TeleScope, SonicScope, and proVISION tools. LWD data were collected from 0 to 117.8 meters below seafloor (mbsf) before the BHA was pulled from the hole because of deteriorating weather conditions.

##### Hole U1518B

Following 21 h of waiting on weather, LWD operations and safety monitoring resumed in Hole U1518B at 1600 h on 21 December 2017 (38°51.5476'S, 178°53.7621'E; 2636.4 mbsl). No LWD data were collected from 0 to 50 mbsf because of human error. LWD continued to a total depth of 600 mbsf. The StethoScope tool was deployed at two stations (234 and 334.7 mbsf); however, both deployments were unsuccessful.

#### Expedition 375 operations

##### Transit to Site U1518

The R/V *JOIDES Resolution* departed from Timaru, New Zealand, at 0728 h (UTC + 13 h) on 11 March 2018 and arrived at Site U1518 at 1900 h on 13 March.

##### Holes U1518C and U1518D

Hole U1518C (38°51.5692'S, 178°53.7616'E; 2631.7 mbsl) was spudded at 0905 h on 14 March 2018 with an advanced piston corer/extended core barrel (APC/XCB) BHA. A full core barrel was retrieved following a partial stroke, and the hole was abandoned to attempt another mudline core. The bit was raised 3 m, and Hole U1518D (38°51.5699'S, 178°53.7634'E; 2628.2 mbsl; 2638.9 meters below rig floor [mbrf]) was spudded at 1020 h. Another full core barrel was retrieved, and this hole was also abandoned.

##### Hole U1518E

The vessel was offset 5 m north, the bit was raised another 3 m, and Hole U1518E was spudded at 1125 h on 14 March 2018 (38°51.5669'S, 178°53.7618'E; 2626.1 mbsl). Cores 1H–32X penetrated from 0 to 175.6 mbsf and recovered 160.96 m (92%). Advanced piston corer temperature tool (APCT-3) formation temperature measurements were taken with Cores 4H, 6H, 8H, 10H, and 14F. The decision was made to switch to coring with the rotary core barrel (RCB) system after discovering that the cutting shoe used with Core 31X had been destroyed after it took 80 min to advance 3.6 m while cutting Core 32X.

##### Hole U1518F

The vessel was offset 5 m south. Hole U1518F (38°51.5694'S, 178°53.7619'E; 2626.1 mbsl) was spudded at 0135 h on 17 March 2018 with an RCB BHA and was advanced without coring to 197.7 mbsf. Cores 2R–32R penetrated from 197.7 to 494.9 mbsf and recovered 126.82 m (43%). Coring was terminated so that observatory operations could start.

##### Hole U1518G

In preparation for installing the observatory, we predrilled Hole U1518G. The vessel was offset 35 m north of Hole U1518F (and ~5 m south of Hole U1518B). A BHA with a 1¼ inch drill bit was lowered to the seafloor, Hole U1518G (38°51.5505'S, 178°53.7617'E; 2629.8 mbsl) was spudded at 1050 h on 20 March 2018, and the hole was advanced without coring to 433 mbsf. Next, a reentry cone and

Table T1. Hole summary, Expeditions 372 and 375. \* = missed mudline, † = observatory installation, ‡ = reentry system installation. Transit to Bay of Plenty to wait on weather not included (see text for details). NA = not applicable. APC = advanced piston corer, HLAPC = half-length APC, XCB = extended core barrel, RCB = rotary core barrel. (Continued on next page.) [Download table in CSV format.](#)

Hole	Latitude	Longitude	Water depth (mbrf)	Total penetration (m)	Drilled interval (m)	Cored interval (m)	Core recovered (m)	Recovery (%)	Total cores (N)
372-									
U1518A	38°51.5368'S	178°53.7606'E	2636.4	117.8	117.8	NA	NA	NA	NA
U1518B	38°51.5476'S	178°53.7621'E	2634.6	600.0	600.0	NA	NA	NA	NA
375-									
U1518C*	38°51.5692'S	178°53.7616'E	2631.7	9.1	NA	9.1	9.13	100	1
U1518D*	38°51.5699'S	178°53.7634'E	2628.2	9.6	NA	9.6	9.61	100	1
U1518E	38°51.5669'S	178°53.7618'E	2626.1	175.6	NA	175.6	160.96	92	32
U1518F	38°51.5694'S	178°53.7619'E	2626.1	494.9	197.7	297.2	126.82	43	31
U1518G	38°51.5505'S	178°53.7617'E	2629.8	433.0	433.0	NA	NA	NA	NA
U1518H†	38°51.5402'S	178°53.7642'E	2631.1	426.5	426.5	NA	NA	NA	NA
U1518H†	38°51.5402'S	178°53.7642'E	2631.1	NA	NA	NA	NA	NA	NA
Site U1518 totals:				2266.5	1775.0	491.5	306.52	62	65
372-									
U1519A	38°43.6372'S	178°36.8537'E	1000.7	650.0	650.0	NA	NA	NA	NA
375-									
U1519B‡	38°43.6426'S	178°36.8655'E	1000.4	285.1	285.1	NA	NA	NA	NA
U1519C	38°43.6483'S	178°36.8773'E	1000.3	640.0	424.4	215.6	119.17	55	23
U1519D	38°43.6516'S	178°36.8831'E	1000.4	23.3	NA	23.3	23.64	101	3
U1519E	38°43.6572'S	178°36.8949'E	1000.3	85.8	NA	85.8	88.98	104	13
Site U1519 totals:				1684.2	1359.5	324.7	231.79	71	39
372-									
U1520A	38°58.1641'S	179°07.9357'E	3521.3	97.9	97.9	NA	NA	NA	NA
U1520B	38°58.1587'S	179°07.9233'E	3520.1	750.0	750.0	NA	NA	NA	NA
375-									
U1520C†	38°58.1532'S	179°07.9112'E	3522.1	646.0	646.0	NA	NA	NA	NA
U1520C	38°58.1532'S	179°07.9112'E	3522.1	408.1	NA	408.1	235.40	58	43
U1520D	38°58.1475'S	179°07.8991'E	3520.3	642.3	126.5	515.8	318.38	62	65
Site U1520 totals:				2544.3	1620.4	923.9	553.78	60	108
375-									
U1526A	39°01.3203'S	179°14.7594'E	2890.1	83.6	NA	83.6	29.26	35	14
U1526B	39°01.3146'S	179°14.7481'E	2888.4	33.5	NA	33.5	31.56	94	5
Site U1526 totals:				117.1	NA	117.1	60.82	52	19
Expedition 372 totals:				2215.7	2215.7	NA	NA	NA	NA
Expedition 375 totals:				4396.4	2539.2	1857.2	1152.91	62	231
Expedition 372 and 375 totals:				6612.1	4754.9	1857.2	1152.91	62	231

mud skirt were released from the moonpool and allowed to free-fall down the drill string to the seafloor.

The first stage of the observatory installation consisted of deploying an ACORK (Figure F4). Between 2000 h on 22 March and 1700 h on 23 March, we assembled a 422 m long ACORK casing string consisting of 10¼ inch casing, three joints with pressure screens, and an umbilical with three ¼ inch diameter tubes secured on the outside of the casing. The umbilical tubes were terminated at the three screens centered at 393, 323, and 218 mbsf to monitor pressure below, within, and above the fault zone, respectively. Next, we assembled a drilling assembly inside the ACORK casing composed of a 9¾ inch drill bit, an underreamer with its arms set to 14¾ inches, and a mud motor to rotate the bit and underreamer in isolation from the casing. Finally, the umbilical tubes were connected to the valves and loggers on the ACORK wellhead, and the entire ACORK assembly was lowered to the seafloor on 24 March. During our attempt to reenter Hole U1518G, unexpected heave caused the drill bit to hit the reentry cone at 1215 h, which resulted in the cone and its base being offset ~3–5 m from the hole and making reentry into the predrilled hole impossible.

#### Hole U1518H observatory

Because the underreamer and drill bit were inside the ACORK casing and the entire assembly was already at the seafloor, the decision was made to drill-in the ACORK assembly at the new location. Hole U1518H (38°51.5402'S, 178°53.7642'E; 2631.1 mbsl) was spudded at 1245 h on 24 March 2018 and reached a total depth of 426 mbsf. Once the ACORK landed in the reentry cone, we deployed a remotely operated vehicle (ROV) platform and a free-fall funnel on top of the ACORK body. The ACORK casing was reentered and cleaned of cuttings on 26 March before a bridge plug was installed on 27 March at 421 mbsf inside the ACORK casing to seal its interior from the formation.

The second stage of the observatory installation consisted of deploying a CORK-II inside the ACORK, but operations were interrupted on 28 March while we waited for the R/V *Tangaroa* to deliver replacement seals. During this period we relocated to Site U1520 to drill-in a reentry system in advance of coring there later during the expedition. We resumed operations in Hole U1518H on 31 March by assembling the 412 m long CORK-II casing string composed of 4½ inch drill pipe, two swellable packer joints, one



Table T1 (continued).

Hole	APC cores (N)	HLAPC cores (N)	XCB cores (N)	RCB cores (N)	Start date	Start time UTC (h)	End date	End time UTC (h)	Time on hole (days)
372-									
U1518A	NA	NA	NA	NA	19 Dec 2017	0330	20 Dec 2017	0300	0.98
U1518B	NA	NA	NA	NA	21 Dec 2017	0300	23 Dec 2017	1345	2.45
375-									
U1518C <sup>†</sup>	1	0	0	0	13 Mar 2018	0630	13 Mar 2018	2047	0.60
U1518D <sup>†</sup>	1	0	0	0	13 Mar 2018	2047	13 Mar 2018	2140	0.04
U1518E	10	15	7	0	13 Mar 2018	2140	16 Mar 2018	0235	2.20
U1518F	0	0	0	31	16 Mar 2018	0235	19 Mar 2018	1210	3.40
U1518G	NA	NA	NA	NA	19 Mar 2018	1210	23 Mar 2018	2345	4.48
U1518H <sup>†</sup>	NA	NA	NA	NA	23 Mar 2018	2345	27 Mar 2018	1145	3.50
U1518H <sup>†</sup>	NA	NA	NA	NA	31 Mar 2018	0245	1 Apr 2018	2015	1.69
Site U1518 totals:	12	15	7	31					
372-									
U1519A	NA	NA	NA	NA	23 Dec 2017	1630	25 Dec 2017	2030	2.17
375-									
U1519B <sup>†</sup>	NA	NA	NA	NA	13 Apr 2018	0618	17 Apr 2018	2255	4.69
U1519C	0	0	0	23	17 Apr 2018	2255	20 Apr 2018	2015	2.89
U1519D	3	0	0	0	20 Apr 2018	2015	21 Apr 2018	0600	0.41
U1519E	8	5	0	0	21 Apr 2018	0600	22 Apr 2018	0112	0.80
Site U1519 totals:	11	5	0	23					
372-									
U1520A	NA	NA	NA	NA	26 Dec 2017	0000	27 Dec 2017	0110	1.05
U1520B	NA	NA	NA	NA	28 Dec 2017	2345	31 Dec 2017	0654	2.30
375-									
U1520C <sup>†</sup>	NA	NA	NA	NA	27 Mar 2018	1400	30 Mar 2018	0030	3.44
U1520C	0	0	0	43	2 Apr 2018	0645	9 Apr 2018	1315	7.27
U1520D	18	11	36	0	24 Apr 2018	0900	1 May 2018	2230	7.56
Site U1520 totals:	18	11	36	43					
375-									
U1526A	0	0	0	14	22 Apr 2018	0530	24 Apr 2018	0835	2.13
U1526B	4	0	1	0	2 May 2018	0630	3 May 2018	0030	0.75
Site U1526 totals:	4	0	1	14					
Expedition 372 totals:	NA	NA	NA	NA					
Expedition 375 totals:	45	31	44	111					
Expedition 372 and 375 totals:	45	31	44	111					

“quadrant seal” joint carrying the seat for the OsmoSampler package, drill collars, and a bullnose. The CORK-II wellhead was attached on 1 April, and the entire assembly was lowered to the seafloor until it reentered the ACORK funnel and the CORK-II wellhead reached ~17 m above the ACORK funnel.

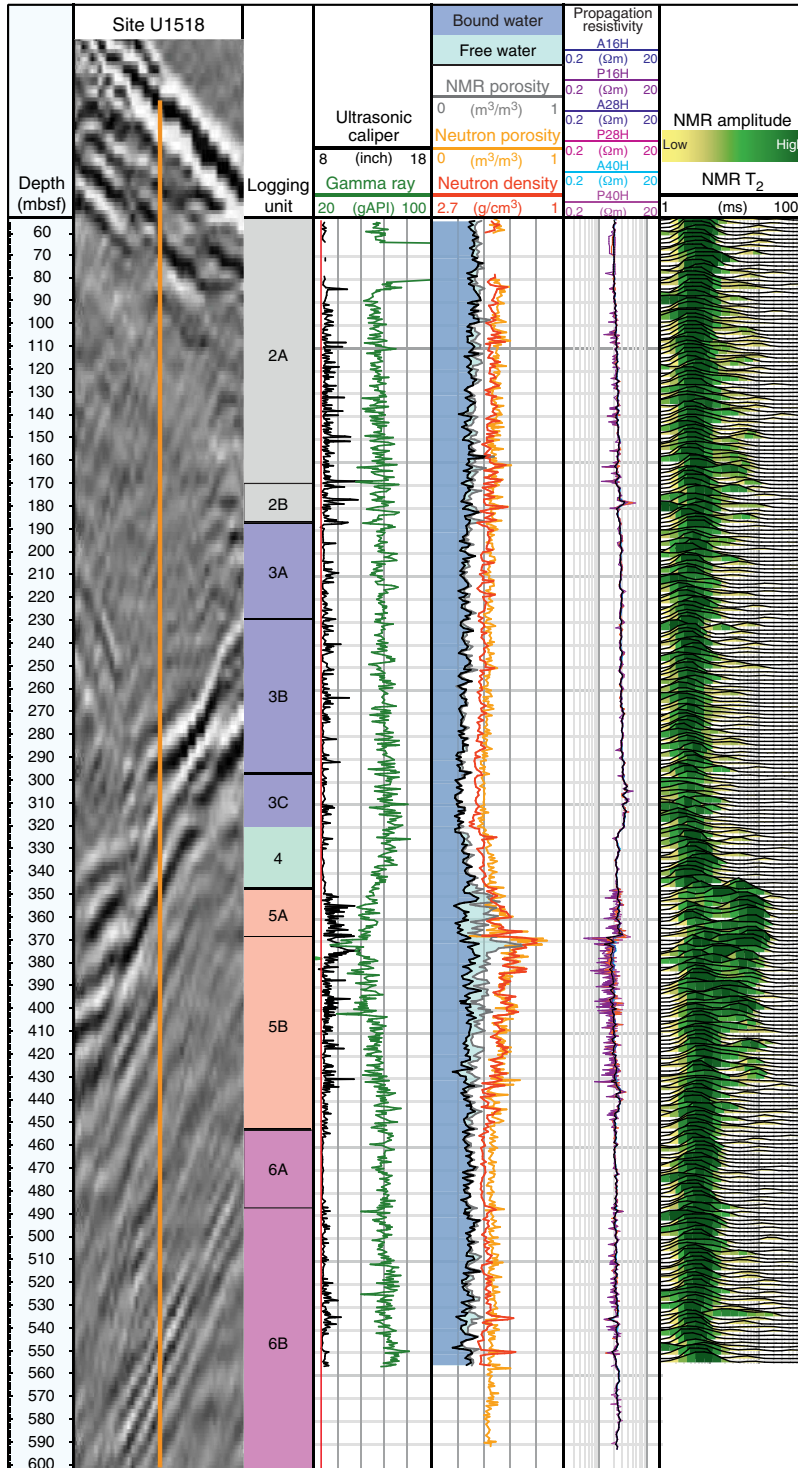
The third stage of the observatory installation consisted of deploying the temperature sensors and OsmoSampler package inside the CORK-II casing string. On 1 April, we assembled the 407 m long instrument string consisting of 3 segments of Spectra rope carrying a total of 23 temperature sensors, the ~22 m long OsmoSampler package with an additional 7 temperature sensors inside, 3 weak links, 4 sinker bars, and a top plug. The instrument string was deployed with the logging wireline. At 2105 h on 1 April, the OsmoSampler package landed in the CORK-II seat at 323 mbsf, followed by the top plug latching inside the CORK-II wellhead. Once the instrument string was released, the CORK-II landed inside the ACORK wellhead at 0020 h on 2 April, completing the observatory installation in Hole U1518H. The time spent at Site U1518 during Expedition 375 was 13.22 days. The total time spent at Site U1518 during both expeditions was 16.62 days.

## Principal results

### Logging while drilling

Six LWD tools were deployed on the BHA (NeoScope, SonicScope, TeleScope, proVISION, geoVISION, and StethoScope) while drilling Holes U1518A (118 mbsf) and U1518B (600 mbsf) during Expedition 372, providing both real-time and recorded-mode data to the targeted depth (Table T1). Based on the LWD physical properties measurements, we identified six main logging units that were divided into subunits based on the observed physical properties characteristics of the sediments (Figure F6). We interpreted numerous significant features from the logs, such as the thrust fault zone and associated sand/silt units. The fault zone, interpreted to be at ~322 mbsf, is associated with a reduction in resistivity and density and an increase in porosity with depth. The hanging wall of the fault is characterized by high *P*-wave and *S*-wave velocities, whereas the footwall is characterized by relatively lower velocities. A high-amplitude seismic reflection interval in the footwall sequence is associated with interpreted sandy sediments characterized by increased borehole washout deeper than 350 mbsf. In this interval, an abrupt

Figure F6. Composite plot of seismic image (Profile 05CM-04) and selected LWD measurements for 50–600 mbsf, Hole U1518B. Prestack depth migration (PSDM) from Barker et al. (2018).

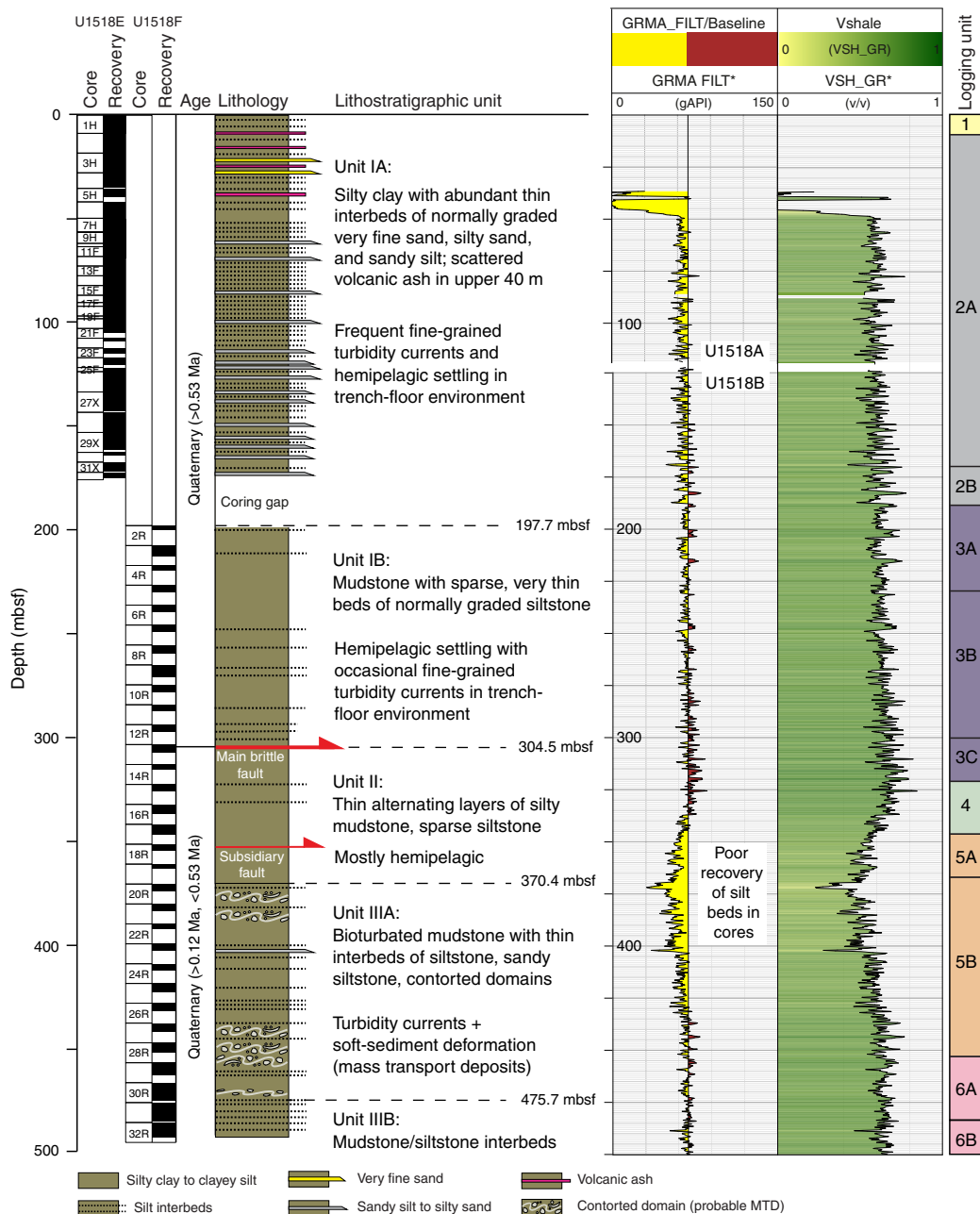


change in physical properties occurs close to 370 mbsf, where we interpret a deeper fault strand. As described in more detail below, clusters of both resistive and conductive fractures were observed in the resistivity images, more commonly in the fault hanging wall sequence. Borehole breakouts oriented approximately north–south were observed toward the base of the hole, from which we infer an east–west maximum horizontal stress direction.

### Lithostratigraphy

At Site U1518, we identified three lithostratigraphic units, two of which (Units I and III) were divided into two subunits (Figure F7). All three units are Quaternary in age. Sediment composition and texture are consistent throughout Holes U1518E and U1518F, with a background of silty clay(stone) or mud(stone) alternating with thin beds of silt(stone) to silty sand(stone). The distinctions

Figure F7. Stratigraphic column, Holes U1518E and U1518F. Filtered gamma ray data are from LWD measurements acquired during Expedition 372. Vshale = shale content estimates.



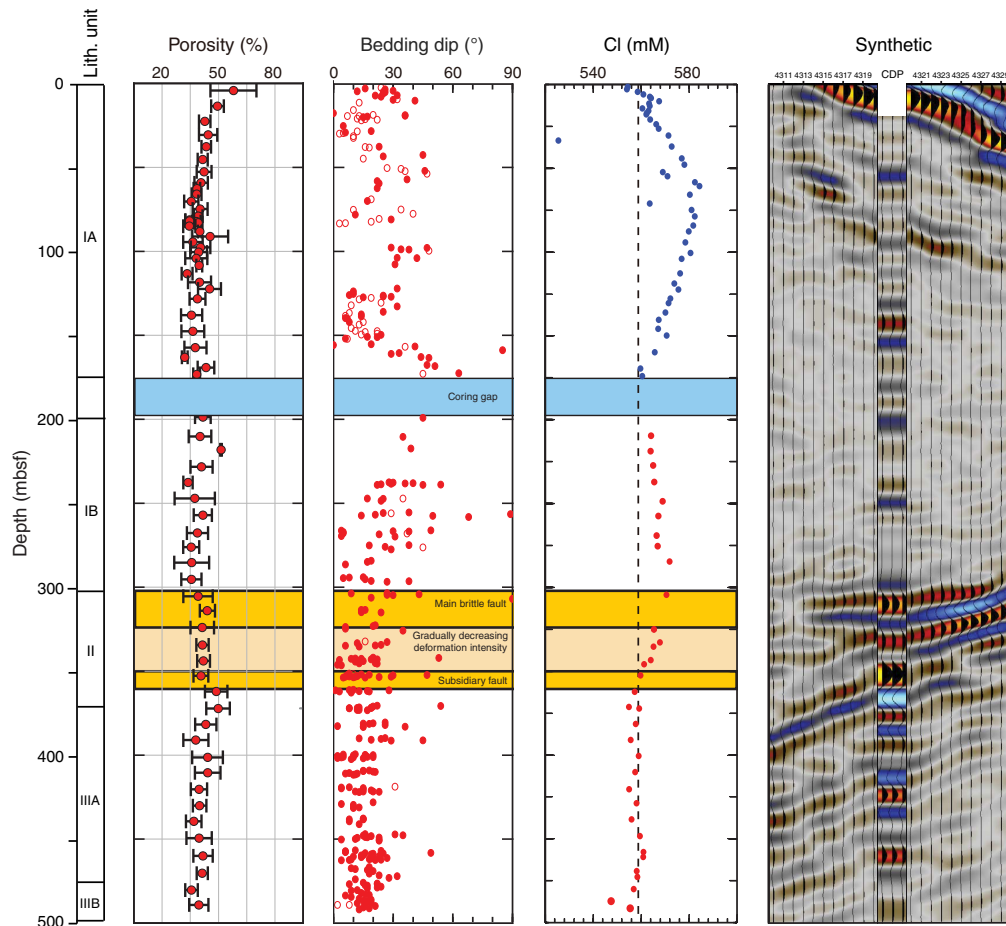
among lithostratigraphic units are based largely on the character of coarser beds inferred to be turbidites and soft-sediment deformation features that are inferred to be MTDs.

The uppermost 2.2 m of Core 375-U1518E-1H consists of unconsolidated Holocene mud. Subunit IA includes this Holocene drape, starts at the seafloor, and extends to 197.7 mbsf. Sediment from Section 1H-CC is older than 0.53 Ma in age, and porosity is lower than expected for the current depth of burial (Figure F8). We therefore consider some of the original stratigraphic section to be missing because of submarine slides or other forms of mass wasting after frontal accretion. The normally graded beds range in grain size from sandy silt to silty sand and very fine sand. We surmise that relatively dilute turbidity currents were interspersed with background

settling of suspended sediment on the trench floor of the Hikurangi Trough. Felsic ash layers also occur in the uppermost 44 m, probably deposited by air fall. Subunit IB extends from 197.7 to 304.5 mbsf and is characterized by sparse and thinner (<10 cm) beds of normally graded siltstone. The subunit boundary is gradational, and its position coincides with the bottom of the zone that was not cored.

Unit II extends from 304.5 to 370.4 mbsf, and its upper boundary matches a significant change in biostratigraphy defined by a thrust-related age inversion with older hanging wall material (older than 0.53 Ma) over younger footwall sediments (younger than 0.53 Ma). We designated this material as a separate lithostratigraphic unit on the basis of a sharp reduction in the number of silty turbi-

Figure F8. Selected drilling results and core-log-seismic tie (synthetic seismic trace), Site U1518. Bedding, fault, and fracture dips: solid dots = high confidence, open dots = low confidence. Chlorinity: blue = Hole U1518E, red = Hole U1518F, dashed line = seawater concentration. CDP = common depth point.



dites and a subtle change in color to lighter greenish gray mudstone. The mudstone in Unit II alternates with thin but sparse layers of siltstone, sandy siltstone, and mud-rich nannofossil ooze.

Unit III begins at 370.4 mbsf and extends to the base of Hole U1518F (492.4 mbsf). This unit is composed of mudstone with thin beds of normally graded siltstone and sandy siltstone; the sediments were deposited by turbidity currents and hemipelagic settling in a trench-floor environment. The most distinctive characteristic of Unit III is soft-sediment deformation that is similar in many respects to what has been described in MTDs from comparable depositional environments elsewhere (e.g., the Nankai Trough). Subunits IIIA and IIIB are separated based on a change in the frequency of the MTD-type features at 475.7 mbsf. The amount of soft-sediment deformation decreases significantly in Subunit IIIB. Intricate varieties of bioturbation also become more widespread and diverse below the subunit boundary.

Broad facies-level comparisons (i.e., packets of beds at a 10+ m scale) can be made between the lithostratigraphy defined from core descriptions and the provisional log-based stratigraphy defined in Holes U1518A and U1518B (see [Logging while drilling](#) in the Site U1518 chapter [Saffer et al., 2019]) (Figure F6). Six logging units were defined for Site U1518 during Expedition 372. The logging unit designations were based on attributes that change in response to deformation structures and physical properties and lithology and bed thicknesses. Closely spaced oscillations in resistivity, nuclear magnetic resonance (NMR), porosity, and gamma ray measure-

ments from Logging Units 2 and 3 are consistent with thinly bedded and uniformly fine grained sediments in Lithostratigraphic Unit I. Unit II (304.53–370.4 mbsf) likely represents lithologies comparable with those in the lower parts of Logging Subunit 3C (229–320.7 mbsf) and Unit 4 (320.7–346 mbsf). The top boundary of Unit II is based largely on the inversion of biostratigraphy rather than a change in lithology, which cannot be detected by logging. In contrast, the Unit III upper and lower boundaries do not match very closely to the boundaries for Units 5 and 6 or their subunits, likely because different sets of criteria were used to define subunits. Recognition of Unit III is based largely on an increase in syn-depositional deformation in the form of contorted domains, which are interpreted to be MTD-type deposits. In contrast, the designations for logging units rely mainly on changes in physical properties and caliper records suggestive of washouts.

#### Biostratigraphy

Planktonic foraminifer and calcareous nannofossil biostratigraphy indicates that the sedimentary sequence recovered from Site U1518 is Holocene to Pleistocene. Biostratigraphic dating indicates a high sedimentation rate of 2.8 m/ky in the Pleistocene section.

The base of the Holocene (younger than 0.011 Ma) was identified between 1.97 and 2.33 mbsf. The underlying section from 2.33 to 296.9 mbsf is from the Middle Pleistocene to possibly early Pleistocene (older than 0.53 Ma). Sediments from 306.95 to 492.26 mbsf are Middle Pleistocene or younger (0.126–0.53 Ma) and represent

an age reversal at the top of the structurally defined thrust fault, as described below (see **Structural geology**) (Figure F7).

Midbathyal benthic foraminifer markers occur throughout the sedimentary sequence, and very rare lower bathyal markers occur in a few samples deeper than 306.95 mbsf. The absence of lower bathyal markers in most samples is unexpected, given that the site was drilled at 2626 mbsl, suggesting that the bulk of the sedimentary sequence has been reworked downslope from midbathyal water depths or shallower. Downslope reworking is supported by the presence of common inner to midshelf taxa in some samples.

#### Paleomagnetism

Routine paleomagnetic analysis included natural remanent magnetization (NRM) measurement of archive halves prior to and following stepwise alternating field (AF) demagnetization to a peak field of 30 mT. Interpretation of the paleomagnetic results was compromised by diagenesis of the primary magnetic mineral phases and extensive tectonic deformation. Some cores also experienced core disturbance that resulted in the complete destruction of any depositional remanence. All XCB cores were affected by significant drilling-induced overprints that could not be removed during routine demagnetization of the archive halves. More extensive AF and thermal demagnetization experiments were conducted on discrete specimens to aid our interpretation.

Inclination records show that the entire sequence recovered from Site U1518 is most likely of normal polarity, despite an interval between 220 and 270 mbsf in which the polarity remains unresolved. Based on biostratigraphic observations, we place the paleomagnetic record in the Brunhes Normal Chron (C1n).

Rock magnetic analyses included determination of the magnetic coercivity distribution based on AF demagnetization, isothermal remanent magnetization acquisition, and magnetic susceptibility measurement. Inferences about the blocking-temperature ( $T_b$ ) distribution of individual samples were drawn from the thermal demagnetization behavior. We tentatively identified at least two magnetic mineral phases. The first phase is a low-coercivity ( $\leq 50$  mT) mineral that we suggest is titanomagnetite. During AF demagnetization experiments, the majority of our samples were affected by the growth of a gyroremanent magnetization at treatment steps higher than 50 mT that we attribute to the presence of secondary greigite.

#### Structural geology

Cores from Hole U1518E are characterized by sediments with gently to moderately dipping beds, although significant drilling-induced deformation in the APC and XCB cores prevents detailed structural observations. RCB cores from Hole U1518F preserve a suite of deformation structures that define the Pāpaku fault zone, which spans from 304.5 to 361.7 mbsf. This zone includes a main brittle fault zone extending from 304.5 to 322.4 mbsf, a subsidiary fault from 351.2 to 361.7 mbsf, and an intervening zone of less intense brittle-ductile deformation.

Gently to steeply dipping beds, locally overturned, were observed in the hanging wall. Variations in bedding dip angles in the hanging wall (Figure F8) generally agree well with LWD image log-derived bedding dips. These beds are crosscut by moderately to steeply dipping fractures that increase in frequency with depth toward the fault zone. Normal faults with centimeter-scale displacements are also preserved at scattered locations throughout the sequence.

The main fault zone includes an upper fault that contains mixed brittle and ductile structures extending to 322.4 mbsf. This interval is characterized by intense brecciation, discrete fractures, and ductile deformed intervals. Several of the ductile deformed zones are overprinted by brittle structures. Deformation intensity decreases gradually with depth, except in a few localized bands, from the base of the main fault zone to a subsidiary fault at 351.2 mbsf (Figure F8). The subsidiary fault is marked by more intense ductile deformation and increased frequency of faults, fractures, and breccias from 351.2 to 361.7 mbsf. There is no clear change in lithology across this subsidiary fault. The ductile deformation is likely a composite of tectonic, syndimentary, and slope processes.

The footwall below 361.7 mbsf is characterized by relatively undeformed hemipelagic sediments with modest and relatively constant dip angles and is cut by a few normal faults and fractures. The generally gentle bedding dips are in good agreement with LWD-derived dips.

Fractures were observed at various depths in the Site U1518 LWD resistivity image logs acquired during Expedition 372 (see **Logging while drilling** in the Site U1518 chapter [Saffer et al., 2019]). Significant fracture clusters were observed between 170 and 230 mbsf, between 315 and 321 mbsf (at a comparable depth, although slightly deeper than those observed in the main fault zone in Hole U1518F; Figure F8), and between 436 and 444 mbsf. These clusters include a mix of conductive and resistive fractures, and overall they exhibit a preferred northwest–southeast strike.

#### Geochemistry

We collected 82 whole-round (WR) samples for pore water chemical analyses at Site U1518. Each core collected deeper than 30 mbsf was scanned with an infrared (IR) camera to identify cold anomalies indicative of potential gas hydrate. The majority of WR samples taken for interstitial water analyses were located away from the IR anomalies to define background chemical profiles not impacted by gas hydrate dissociation during core recovery. A small subset of samples co-located with the IR cold anomalies were analyzed to quantify gas hydrate saturations based on the deviation of dissolved chloride concentrations from the background profile. Drilling fluid was also analyzed as part of the shipboard geochemical program to identify potential contamination; below the sulfate–methane transition zone (SMTZ), sulfate is depleted in the pore water and any sulfate present in a sample is interpreted to be the result of contamination. Based on  $\text{SO}_4$  concentrations below the SMTZ, we corrected all pore water species in each sample for drilling contamination.

The pore fluid chemical profiles at Site U1518 reflect the combined effects of microbially mediated organic matter degradation, authigenic carbonate precipitation, volcanic ash alteration, and silicate mineral diagenesis. Sulfate concentration decreases approximately linearly from 28.1 mM at 1.5 mbsf to below detection limit (0.1 mM) at ~8 mbsf. The SMTZ is marked by a concomitant increase in headspace methane concentration from 51 to 5461 parts per million by volume (ppmv). The SMTZ is shallower at this site than at nearby Site U1517 (drilled during Expedition 372 [Barnes et al., 2019a]), which likely indicates a larger vertical methane flux. Ethane was detected in some headspace samples shallower than 200 mbsf but was not detected deeper. Methane/ethane ratios are  $>20,000$ , suggesting a microbial origin of the methane.

Alkalinity, ammonium, bromide, and phosphate concentration profiles also reflect organic matter diagenesis, with peaks in Litho-

stratigraphic Subunit IA followed by decreases in Subunit IB. The fault zone coincides with repetition of the diagenetic sequence in the footwall, with a second peak in alkalinity, ammonium, and phosphate concentrations in Unit III. Based on the deviation of Cl concentration from the background concentration profile, we identified the presence of gas hydrate in six WR samples.

Chloride, potassium, and sodium concentrations increase with depth and reach concentration maxima at ~60 mbsf in Lithostratigraphic Subunit IA. Likewise, silica, lithium, and strontium concentrations steadily increase in Subunit IA and then decrease between the top of Subunit IB and the top of the fault zone at ~300 mbsf. Subunit IA sediments contain several volcanic ash layers and disseminated ash and have elevated K-feldspar concentrations. The increase in pore water Cl, alkali metal, and strontium concentrations in this unit likely reflects ongoing alteration of rhyolitic ash and K-feldspar to authigenic hydrous aluminosilicate minerals. Similar to the geochemical tracers of organic matter diagenesis discussed above, clear repetition of the ash/silicate mineral diagenetic sequence occurs at the fault zone.

Solid-phase analyses yielded calcium carbonate ( $\text{CaCO}_3$ ) content ranging from 2.1 to 23.1 wt%. Total organic carbon (TOC) content is generally low and ranges from 0.1 to 0.88 wt%. C/N ratios range from 0.85 to 15.80 (average = 6.84). Localized peaks in C/N ratios occur in Lithostratigraphic Unit II, suggesting some heterogeneity in organic matter sources in this depth interval.

#### Physical properties

An abrupt change in physical properties occurs between 0 and 50 mbsf in Hole U1518E and includes a shift to lower porosity, concomitant higher bulk density, and higher *P*-wave velocity. Deeper than 50 mbsf, all physical properties remain nearly constant with depth, with a few distinct exceptions. The depth trends of bulk density, porosity, *P*-wave velocity, undrained shear strength, and natural gamma radiation (NGR) measured in the cores are generally less pronounced than the trends in LWD bulk density, neutron porosity, *P*-wave velocity, and gamma ray data.

Porosity decreases from 65% to 50% in the uppermost 50 m. Between 50 and 495 mbsf, porosity is nearly constant and ranges from 40% to 50% (Figure F8). *P*-wave velocity is ~1500 m/s near the seafloor, increases rapidly to 1600 m/s at 2 mbsf, and then remains approximately constant at 1600 m/s between 2 and 12 mbsf. Deeper than 238 mbsf, *P*-wave velocity values are scattered and range from ~1500 to ~2000 m/s. Undrained shear strength increases with depth (albeit with significant scatter) to an average of 120–200 kPa at 200–280 mbsf and decreases to an average of 60–100 kPa by 300 mbsf. Deeper than 450 mbsf, strength increases again (with significant scatter) to values as high as 400–500 kPa.

NGR ranges from 6 to 63 counts/s, with an average of 42 counts/s. NGR increases rapidly from <25 counts/s at the seafloor to 40 counts/s at 2 mbsf and remains nearly constant with depth. Magnetic susceptibility is correlated with the lithostratigraphic units. The interval between 2 and 176 mbsf (in Lithostratigraphic Subunit IA) is characterized by zones of low magnetic susceptibility and less scatter, with an average magnetic susceptibility of  $11 \times 10^{-5}$  to  $14 \times 10^{-5}$  SI (at 2–12, 40–60, and 75–109 mbsf) and intervening zones of high magnetic susceptibility and more scatter, with an average of  $22 \times 10^{-5}$  to  $25 \times 10^{-5}$  SI (at 13–40, 60–75, and 109–176 mbsf). Between 197.7 and 462 mbsf, from the top of Subunit IB to the bottom of Subunit IIIA, magnetic susceptibility exhibits some scatter, ranging from  $10 \times 10^{-5}$  to  $20 \times 10^{-5}$  SI, but with less scatter than that observed in Subunit IA. Magnetic susceptibility shifts to a

lower average value of  $13 \times 10^{-5}$  SI at 466 mbsf and remains constant to 495 mbsf (in Subunit IIIB). Thermal conductivity is relatively constant with depth, with an average of  $1.38 \pm 0.10$  W/(m·K).

#### Downhole measurements

Five formation temperature measurements were made with the APCT-3 in Hole U1518E with Cores 4H, 6H, 8H, 10H, and 14F. Although all five measurements are high quality, an offset occurs between the three measurements taken with one sensor and the two taken with another sensor. We estimate a thermal gradient of  $0.035^\circ\text{C}/\text{m}$  using three equilibrium temperatures from one of these tools. The vertical conductive heat flow computed as the product of the thermal gradient and thermal conductivity is  $48 \text{ mW}/\text{m}^2$ . The temperature over the depth window corresponding to the Pāpaku fault zone is estimated to be  $12^\circ\text{--}13^\circ\text{C}$ .

#### Core-log-seismic integration

LWD data from Holes U1518A and U1518B (Figure F6) were correlated with core-based observations and physical properties measurements from Holes U1518E and U1518F and with seismic reflection data across the holes drilled at Site U1518. These different data sets detect variations in physical properties, lithology, and structure at a range of scales. LWD *P*-wave velocity and density measurements were combined with density measurements from the cores to develop a synthetic seismic trace to correlate the LWD, core, and seismic data. The synthetic seismic trace using the LWD data correctly predicts moderate-amplitude reflections in the upper 80 m, low-amplitude reflections to ~300 mbsf, and a package of high-amplitude reflections between 300 and 400 mbsf (Figure F8).

However, a significant reduction in LWD density and velocity around 322 mbsf (Figure F6) produced a high-amplitude reversed polarity reflection in our synthetics that is ~15–20 m too deep relative to the observed high-amplitude reversed polarity reflection in Seismic Profile 05CM-04 at the Hole U1518F location. This high-amplitude reflection separates truncated dipping reflections above from continuous parallel reflections below. Physical properties values from cores show a reduction in density around 300–315 mbsf, which is shallower than that observed in the LWD data (Figure F8). Together, the core and seismic data suggest that the fault zone in the Hole U1518F cored section lies 15–26 m shallower than the same change in properties identified in the Hole U1518B LWD data. This suggestion is supported by a better matching synthetic seismic trace when the LWD reduction in density and velocity is shifted 15 m shallower (Figure F8). The difference in fault zone depth between Holes U1518F and U1518B (located ~40 m apart) is likely due to thrust fault geometry.

## Site U1519

#### Background and objectives

Site U1519 is located on the upper continental slope ~38 km from shore in ~1000 m water depth at the landward edge of a mid-slope sedimentary basin (Figures F2, F3; Table T1) (see the [Site U1519](#) chapter [Barnes et al., 2019b]). On the basis of regional stratigraphic and seismic interpretations prior to drilling, we expected to penetrate 260–270 m of horizontally layered late Quaternary basin fill comprising MTDs and layered sequences, including probable turbidites, underlain by a Pliocene–Pleistocene slope sequence of MTDs and layered sequences, also about 260–270 m thick, dipping to the southeast. The base of this sequence is marked by an apparent erosional unconformity identified in the seismic reflection data at ~540 mbsf. Beneath the unconformity, we expected

to penetrate Miocene sedimentary rocks (equivalent to the Tolaga Group exposed onshore) in seismically reflective landward-dipping strata (Figure F2).

The primary objective at Site U1519 was installation of an observatory to monitor pore fluid pressure and temperature, as described above. The observatory includes two levels of pressure sensing via hydraulic lines that terminate in screens at 124 and 264 mbsf. Temperature sensing is achieved by a string of 15 autonomous high-resolution temperature sensors. LWD in Hole U1519A during Expedition 372 penetrated to 650 mbsf. Drilling at Site U1519 during Expedition 375 included RCB coring in discrete intervals (108–163.6, 250–288.4, and 520–640 mbsf; Hole U1519C) and APC coring from the seafloor to 85.8 mbsf (Holes U1519D and U1519E). The main logging and coring objectives at this site were to provide information about rock physical properties, composition, and structural geology and deformation in the upper plate above the SSE source region. APCT-3 measurements of temperature in Holes U1519D and U1519E define a temperature gradient and provide key constraints on the thermal regime of the slow slip source region. Pore water geochemistry data provide insights into diagenetic processes and potential fluid sources and flow pathways in the hanging wall.

One key focus for post-expedition studies on core samples will be geomechanical measurements to define poroelastic and strength properties of the formation. These data will be essential for interpretation of observatory data, such as calibrating the use of pore pressure as a proxy for volumetric strain (e.g., Wang, 2004; Araki et al., 2017). Similarly, strength, permeability, and elastic moduli measurements will provide important context for interpretation of borehole failures as indicators of in situ stress magnitude (e.g., Chang et al., 2010; Huffman and Saffer, 2016), parameterization of hydrological models, and core-log-seismic integration. Detailed analyses of wellbore failures identified in the LWD data may reveal contemporary maximum and minimum horizontal stress orientations. Comparison of these data with similar stress determinations elsewhere along the Hikurangi margin will enable evaluation of regional variations in current stress state across the margin. Thermal properties measurements will be used in combination with observatory temperature data to define heat flow and to interpret thermal transients in the context of heat conduction and possible advection.

### Expedition 372 operations

#### Transit to Site U1519

The vessel arrived at Site U1519 (proposed Site HSM-01A [Saffer et al., 2017]) at 0530 h (UTC + 13 h) on 24 December 2017 after a 15.4 nmi transit from Site U1518.

#### Hole U1519A

Hole U1519A (38°43.6372'S, 178°36.8537'E; 1000.7 mbsl) was spudded at 1200 h on 24 December 2017. The LWD BHA contained the geoVISION, NeoScope, TeleScope, SonicScope, and proVISION tools. LWD data were collected from 0 to 650 mbsf with 24 h safety monitoring.

### Expedition 375 operations

#### Transit to Site U1519

We arrived at Site U1519 at 1810 h (UTC + 12 h) on 13 April 2018 after waiting on weather conditions to improve in the Bay of Plenty.

#### Hole U1519B observatory

In preparation for installing the observatory, we predrilled the observatory hole. A BHA with a 14¼ inch drill bit was lowered to the seafloor. Hole U1519B (38°43.6426'S, 178°36.8655'E; 1000.4 mbsl) was spudded at 0105 h on 14 April 2018 and advanced without coring to 283 mbsf. Next, a reentry cone and mud skirt were released from the moonpool and allowed to free-fall down the drill string to the seafloor.

The first stage of the observatory installation consisted of deploying an ACORK (Figure F4). Between 0115 and 1245 h on April 15, we assembled a 279 m long ACORK casing string consisting of 22 joints of 10¼ inch casing, two casing joints with 2 m long screens for pressure monitoring, and an umbilical with three ¾ inch diameter tubes (only two of which were used) secured on the outside of the casing. The umbilical tubes were terminated at the two screens centered at 124 and 264 mbsf. Next, we assembled a drilling assembly inside the ACORK casing composed of a 9¾ inch drill bit, an underreamer with its arms set to 14¾ inches, and a mud motor to rotate the bit and underreamer in isolation from the casing. Finally, the umbilical tubes were connected to the valves and loggers on the ACORK wellhead, and the entire ACORK assembly was lowered to the seafloor at 2130 h on 15 April. Hole U1519B was reentered at 2310 h, and the ACORK wellhead landed in the reentry cone on the seafloor at 0635 h on 16 April. Once the ACORK was released, we deployed a free-fall funnel on top of the ACORK body. The ACORK casing was reentered with a 9¾ inch drill bit and cleaned of cuttings on 16 April before a bridge plug was installed on 17 April inside the ACORK casing at 277 mbsf to seal its interior from the formation below.

The second stage of the observatory installation consisted of deploying a CORK-II inside the ACORK. The 269 m long CORK-II casing string consisted of 20 full joints and four pup joints of 4½ inch casing, four 6¾ inch drill collars, and a bullnose. The CORK-II wellhead was attached, the entire assembly was lowered to the seafloor, and it reentered the ACORK funnel at 0120 h on April 18. We lowered the CORK-II wellhead until it reached a position ~20 m above the ACORK funnel.

The third stage of the observatory installation consisted of deploying a string of temperature sensors inside the CORK-II casing. At 0230 h on 18 April, we started assembling the 268 m long instrument string consisting of a top plug, a single segment of Spectra rope with 15 temperature sensors, one weak link, and one sinker bar. The instrument string was deployed using the logging wireline, and the top plug latched inside the CORK-II wellhead at 0530 h on 18 April. Once the instrument string was released, the CORK-II landed inside the ACORK wellhead and was released at 0735 h on 18 April, completing the observatory installation in Hole U1519B.

#### Hole U1519C

The primary coring objective at Site U1519 was to sample sediment in the intervals surrounding the ACORK pressure screens, which are centered at 124 and 264 mbsf, and in the sedimentary section from ~520 to 640 mbsf. The vessel was offset 20 m from Hole U1519B at a heading of 122°, and Hole U1519C (38°43.6483'S, 178°36.8773'E; 1000.3 mbsl) was spudded at 1640 h on 18 April 2018. Drilling without coring continued to 108 mbsf until 0600 h on 19 April. RCB Cores 2R–7R, 9R–12R, and 14R–26R advanced from 108.0 to 640.0 mbsf and recovered 119.17 m (55%). Intervals 163.6–250.0 and 288.4–518.4 mbsf were drilled without coring. The drill

string was recovered at 0815 h on 21 April, and the RCB BHA was put away.

#### Hole U1519D

The final objective at Site U1519 was to core the shallow sedimentary section and collect in situ temperature measurements with the APCT-3. The vessel was offset 10 m at a heading of 122°, and Hole U1519D (38°43.6516'S, 178°36.8831'E; 1000.4 mbsl) was spudded at 1505 h on 21 April 2018. APC Cores 1H–3H advanced from 0 to 23.2 mbsf and recovered 23.64 m (101%). Nonmagnetic core barrels were used for all APC cores. Because coarse unconsolidated material made it difficult to collect in situ temperature measurements and resulted in a partial stroke and significant overpull with Core 3H, we started a new hole.

#### Hole U1519E

The vessel was offset 20 m at a heading of 122°, and Hole U1519E (38°43.6572'S, 178°36.8949'E; 1000.3 mbsl) was spudded at 1845 h on 21 April 2018. APC Cores 1H–8H and HLAPC Cores 9F–13F advanced from 0 to 85.8 mbsf and recovered 88.75 m (103%). Nonmagnetic core barrels were used for all cores. Formation temperature measurements were taken with the APCT-3 for Cores 4H–8H, 9F, 11E, and 13F. The time spent at Site U1519 during Expedition 375 was 8.79 days. The total time spent at Site U1519 during both expeditions was 10.96 days.

### Principal results

#### Logging while drilling

Hole U1519A was logged to the target depth of 650 mbsf. Six LWD tools were deployed on the BHA (NeoScope, SonicScope, TeleScope, proVISION, geoVISION, and StethoScope) while drilling Hole U1519A, providing both real-time and recorded-mode data. Based on the LWD measurements, three main logging units and ten subunits were identified (Figure F9). From 140 to 220 mbsf, significant low values of NGR, resistivity, and velocity caused by washout of the borehole are associated with an inferred increase in sand content. Other similar intervals are recognized near 300 and 450 mbsf. Deeper than 550 mbsf (coinciding with an unconformity identified in the seismic data), resistive layers are well identified in the imaged interval. The intervals are characterized by high resistivity and velocity spikes. Bedding features show varied dips and dip directions throughout the borehole. Fractures are generally sparse throughout the borehole but include a notable high-density cluster just below ~230 mbsf. Borehole breakouts identified from 597 to 650 mbsf are oriented approximately northeast–southwest, inferring a maximum horizontal stress ( $S_{Hmax}$ ) directed northwest–southeast.

#### Lithostratigraphy

We identified two lithostratigraphic units at Site U1519 (Figure F10). Detailed characterization of lithofacies was hampered by large coring gaps, poor recovery, and pervasive coring disturbance. Overall, the sedimentary strata range in age from Holocene to early Pleistocene. Common lithologies include mud(stone), silt(stone), and sand(stone).

Coring started at the seafloor in Holes U1519D and U1519E and at 108 mbsf in Hole U1519C, in Lithostratigraphic Unit I. Cores from this depth range contain a background of dark greenish gray mud and mudstone (silty clay to clayey silt) with variable levels of consolidation. Seismic reflection records and high-resolution bathymetry are indicative of shallow mass transport remobilization

at Site U1519. However, APC cores from Holes U1519D and U1519E reveal no definitive indicators of gravity-driven, soft-sediment deformation in the hemipelagic mud.

The Lithostratigraphic Unit I/II boundary at 282.66 mbsf displays a noticeable change in color from dark greenish gray above to light greenish gray below, and the grain size coarsens somewhat to silt-rich mudstone. A positive excursion in magnetic susceptibility also occurs. Below a 230 m gap in coring, mudstone is present with scattered thin interbeds of dark gray sandy siltstone to very fine sandstone. In Cores 375-U1519C-19R, 21R, and 22R, the mudstone displays clear evidence of soft-sediment deformation, including convolute laminae, mesoscale folds, dismembered bedding, and clasts of mudstone supported by a mudstone matrix. We interpret the deformed zones to be intraformational MTDs. The remainder of Unit II consists of consolidated greenish gray mudstone interbedded with poorly indurated sandy silt and sand, ranging in size up to coarse sand. Core 23R contains a distinctive matrix-supported conglomerate with widely dispersed clasts of mudstone and intact shells of what appear to be shallow-water fauna.

#### Biostratigraphy

Calcareous nannofossil and planktonic foraminifer species indicate that the sedimentary sequence recovered at Site U1519 is Holocene to Pleistocene (Figure F10). The base of the Holocene was identified between 4.40 and 14.00 mbsf. The underlying section to 536.32 mbsf is dated Late to Middle Pleistocene (0.011–0.62 Ma), indicating a sedimentation rate of ~0.84 m/ky. Deeper than 536.41 mbsf to the base of Hole U1519C, the age is poorly constrained but is likely early Pleistocene or younger (younger than 1.73 Ma).

Highly variable planktonic foraminifer abundances in the upper part of the section (0–536.32 mbsf) fluctuate between outer neritic and oceanic values. This variability is attributed to downslope reworking, evident from the co-occurrence of inner shelf benthic taxa and shell fragments with bathyal markers. In the lower part of the section (546.86–635.6 mbsf), benthic markers indicate deposition in mid–lower bathyal or deeper water depths.

#### Paleomagnetism

Paleomagnetic analyses at Site U1519 were compromised by severe core disturbance that destroyed the depositional remanence in the majority of cores. We thus only analyzed RCB cores from deeper than 525 mbsf in Hole U1519C and APC cores from Holes U1519D and U1519E. Cores 375-U1519C-14R through 26R were subjected to stepwise AF demagnetization to peak fields of 30 or 40 mT. Overprinting of the primary NRM, most likely by diagenetic alteration, and deformation in MTD intervals made it difficult to interpret the magnetostratigraphy.

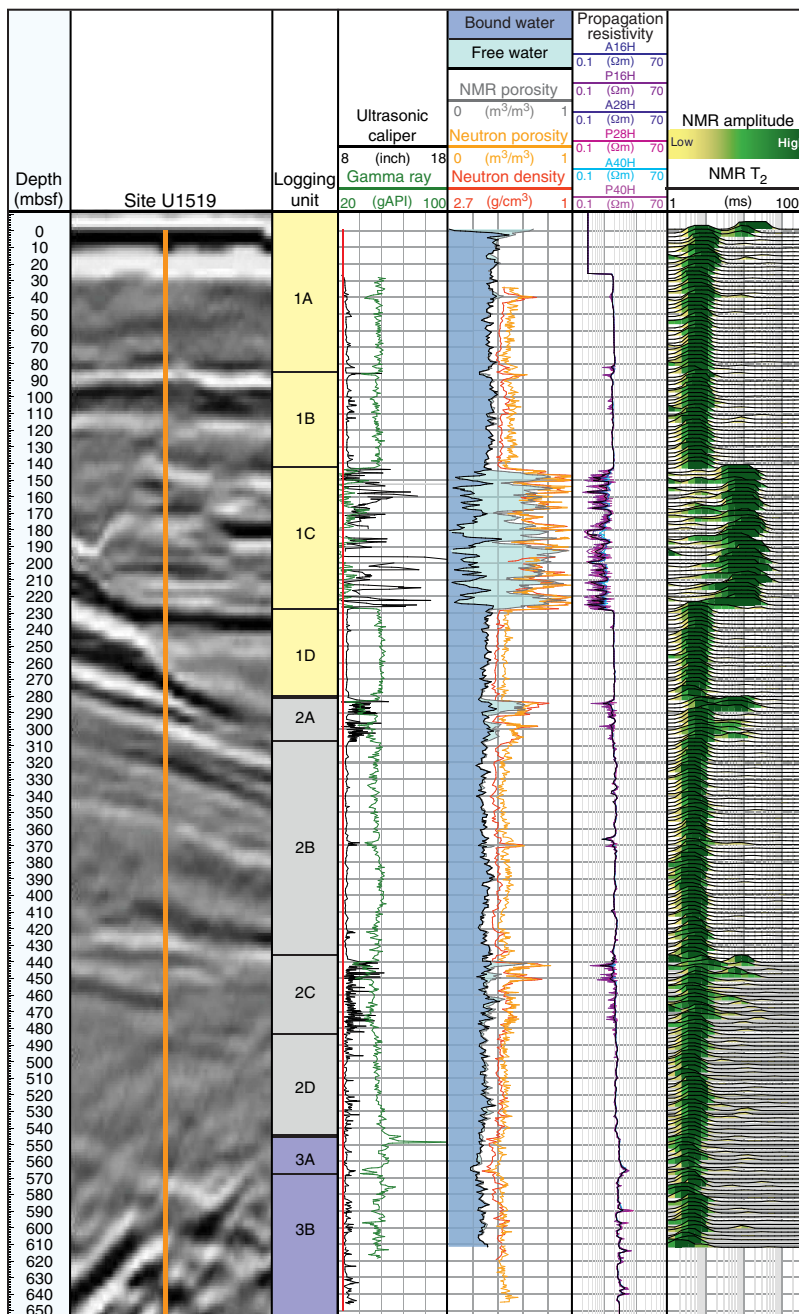
Hole U1519D and U1519E cores were subjected to AF demagnetization to a peak field of 20 mT, which was sufficient to remove a small viscous overprint. The NRM directions usually have negative inclinations that agree with the directions expected for a normal polarity field. However, the data have not been corrected for core disturbance, and many APC sections were affected by significant drilling-induced bed drag. As a result, downhole variations in NRM directions do not necessarily reflect temporal variations in the magnetic field during sediment deposition.

#### Structural geology

Intense drilling disturbance, coring gaps, and poor recovery in cored intervals hampered recognition of structural features in cores. However, dip data from LWD image logs provide useful con-



Figure F9. Composite plot of seismic image (Profile 05CM-04) and selected LWD measurements, Site U1519. PSDM from Barker et al. (2018).

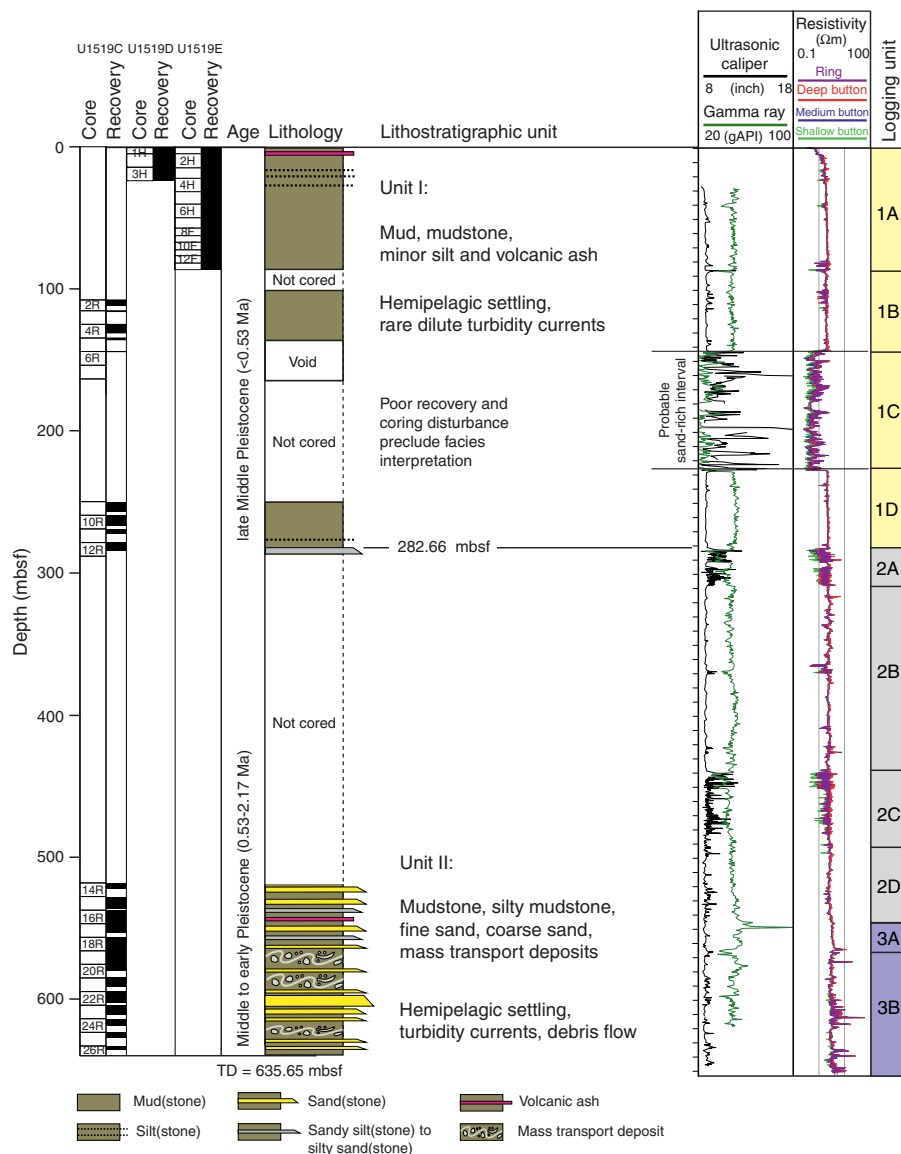


text for observations of core structures (Figure F11). Much of the strata at Site U1519 are inclined, although bed dips rarely exceed 50° in the cored intervals. Steeper beds are recorded in folded strata, which likely represent MTDs. We defined two structural domains based on structures in the core and LWD data. In Domain 1 (0–567.58 mbsf), bedding dips are dominantly steep, and scattered, steep, dominantly conductive fractures are present in the LWD resistivity image logs. Filled fractures are abundant in the lower recovered interval of Domain 1. Domain 2 (567.58–635.6 mbsf) coincides with the bottom of lithostratigraphic Unit II and is defined by a decrease in the number of filled fractures, a slight shallowing of bedding dips in core, and a change in regional dip azimuth from north-northeast toward the north-northwest.

### Geochemistry

In total, 100 WR samples were collected and squeezed for ship-board and shore-based pore water geochemical analyses. The geochemical profiles at Site U1519 reflect the combined effects of organic matter diagenesis, authigenic carbonate precipitation, and silicate mineral/volcanic ash alteration in response to rapid sedimentation. The pore water sulfate, alkalinity, ammonium, bromide, and phosphate profiles in Lithostratigraphic Unit I show changes with depth that are characteristic of organic matter degradation. The shallow pore water sulfate profiles in Holes U1519D and U1519E are S-shaped, indicating a recent period of rapid sedimentation that is also indicated by the alkalinity profile between the seafloor and the SMTZ.

Figure F10. Stratigraphic column, Holes U1519C–U1519E. Gamma ray, caliper, and resistivity are from LWD measurements acquired during Expedition 372. TD = total depth.



A sharp increase in ammonium, alkalinity, phosphate, and bromide concentrations occurs across the Lithostratigraphic Unit I/II boundary, indicating that a second concentration maximum occurs in Unit II. The exact depth of this second concentration maximum is unknown because of the coring gap between 285 and 520 mbsf. The concentrations of these species, which are related to organic matter diagenesis, remain elevated in the interval from 520 to 635 mbsf but decrease with depth.

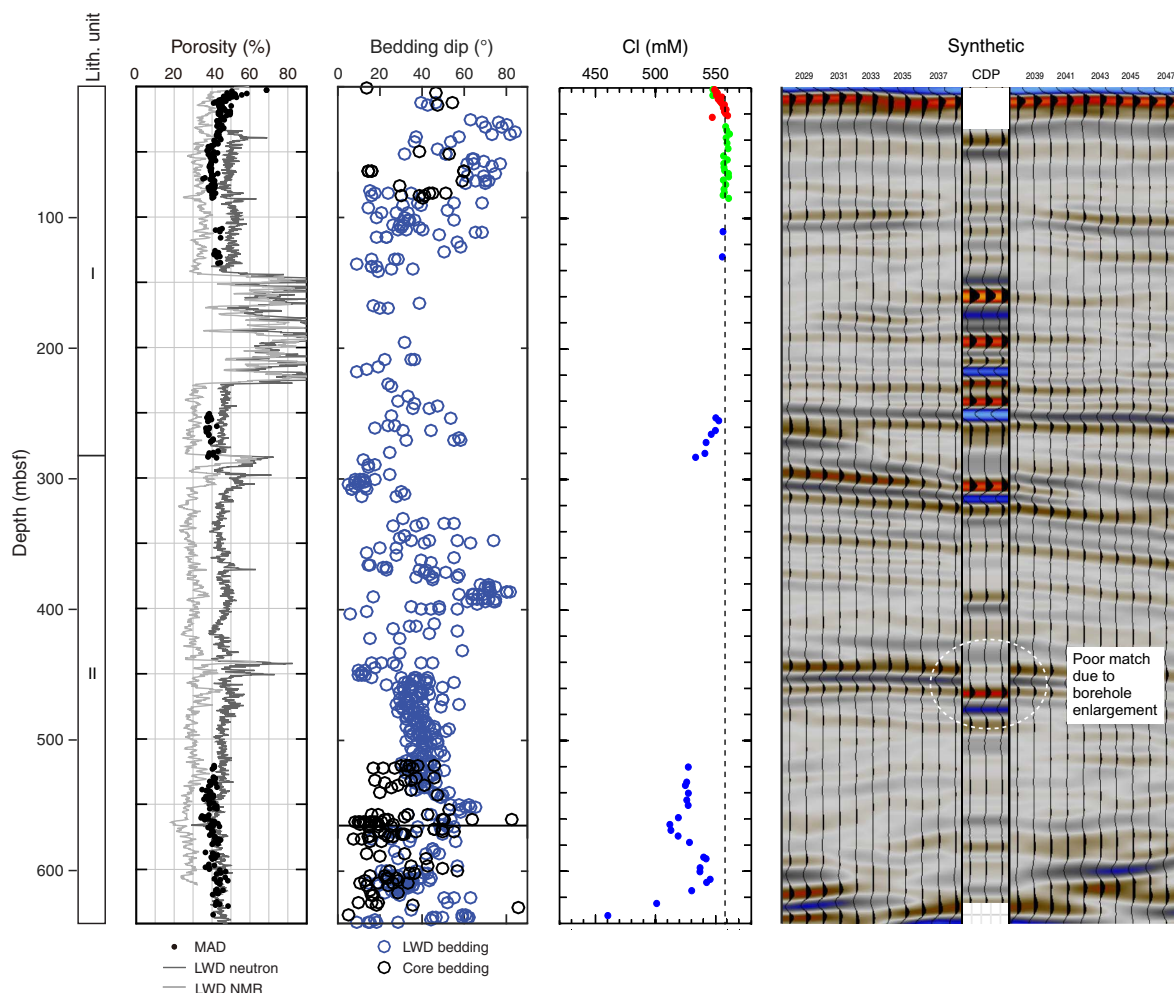
Dissolved calcium concentration decreases sharply from 9.5 mM at 1.4 mbsf to 3.8 mM at the SMTZ. Below the SMTZ, calcium concentration increases to 6.3 mM at 70 mbsf. The reversal in the Ca profile below the SMTZ suggests enhanced silicate mineral/volcanic ash alteration in the zone of microbial methanogenesis, leading to a net addition of Ca to the pore water despite concurrent removal in authigenic carbonates. Likewise, strontium concentration increases below the SMTZ to 130  $\mu$ M (50% higher than seawater value), boron concentration increases to ~750  $\mu$ M (79% higher than seawater value), and potassium concentrations steadily

decrease, consistent with silicate and/or volcanic ash diagenesis in the upper 100 m of Unit I. A second interval of enhanced silicate mineral/volcanic ash diagenesis occurs between 520 and 630 mbsf in Unit II.

Chloride concentration is lower than average modern seawater value (559 mM) in the upper portion of Lithostratigraphic Unit I, increasing from 549 mM at 1.4 mbsf (2% lower than average seawater value) to 559 mM at 17 mbsf. Between 17 and 120 mbsf, Cl concentration remains relatively constant at or near a seawater value. Chloride concentration decreases from 550–534 mM across the Unit I/II boundary to 440–546 mM between 520 and 630 mbsf. Discrete anomalies in the Cl profile at 520–630 mbsf are the result of gas hydrate dissociation during core recovery, marking zones of elevated gas hydrate concentrations. However, background Cl concentration is also lower at 520–630 mbsf.

Between the seafloor and 144.3 mbsf, headspace methane concentrations range between 0.55 and 5172.48 ppmv. Deeper than 144.3 mbsf, methane concentration decreases and remains between

Figure F11. Selected drilling results and core-log-seismic tie (synthetic seismic trace), Site U1519. Chlorinity: red = Hole U1519D, green = Hole U1519E, blue = Hole U1519C, dashed line = seawater concentration.



212.28 and 1802.82 ppmv, with an average of 1011.35 ppmv. Ethane was detected in headspace samples deeper than 520.53 mbsf and ranges between 0.25 and 1.92 ppmv. Methane/ethane ratios are consistently >500, indicating a dominantly microbial methane source. Organic carbon values in Lithostratigraphic Units I and II range from 0 to 1.2 wt% (average = 0.39 wt%). Inorganic carbon and total nitrogen contents increase slightly with depth in both lithostratigraphic units and range from 0.05 to 1.95 wt% (average = 1.1 wt%) and from 0.00 to 0.09 wt% (average = 0.05 wt%), respectively. C/N ratios range from 0.85 to 14.92.

#### Physical properties

NGR, magnetic susceptibility, gamma ray attenuation (GRA) bulk density, and *P*-wave velocity were measured using the Whole-Round Multisensor Logger (WRMSL). Thermal conductivity was measured on WR core sections. Discrete *P*-wave velocity, moisture and density (MAD), and undrained shear strength were measured on working halves. MAD porosity values decrease from 74% near the seafloor to ~40% at 85 mbsf (Figure F11). At 109–135 and 250–284 mbsf, porosity values are nearly constant at 41%–45% and 37%–43%, respectively. Between 520 and 635 mbsf, porosity increases slightly with depth and ranges between 34% and 48%. Although cor-

ing was conducted only in isolated intervals, MAD porosity and density values are in good agreement with those from LWD. *P*-wave velocity values range from 1500 to 1600 m/s between 0 and 10 mbsf, but the data are unreliable for the rest of the borehole.

Undrained shear strength increases linearly from 0 to ~180 kPa with an average depth-dependent gradient of 2.5 kPa/m between 0 and 85 mbsf in Holes U1519D and U1519E. In Hole U1519C, shear strength remains mostly constant, with average values of ~62 kPa between 105 and 140 mbsf, 30–300 kPa between 250 and 290 mbsf, and 54–1104 kPa between 515 and 555 mbsf. NGR ranges from ~0 to 70 counts/s in Hole U1519C and is relatively uniform through the cored intervals, with an average of 40 counts/s. Magnetic susceptibility is nearly constant between 0 and 150 mbsf and ranges from  $10 \times 10^{-5}$  to  $30 \times 10^{-5}$  SI, except for a few ash layers where magnetic susceptibility reaches as much as  $300 \times 10^{-5}$  SI. Between 250 and 283 mbsf, magnetic susceptibility ranges from  $15 \times 10^{-5}$  to  $20 \times 10^{-5}$  SI and increases to  $40 \times 10^{-5}$  to  $50 \times 10^{-5}$  SI at 283 mbsf, which corresponds to the Lithostratigraphic Unit I/II boundary. Thermal conductivity ranges from 0.8 to 1.6 W/(m-K) between the seafloor and 80 mbsf. Between 109 and 135 mbsf, thermal conductivity is uniform at ~1.3 W/(m-K). Deeper than 250 mbsf, thermal conductivity increases to ~1.4 W/(m-K).

### Downhole measurements

Formation temperature measurements were taken with the APCT-3 with Cores 375-U1519E-4H through 8H, 9F, 11E, and 13F. The APCT-3 measurements yield in situ temperature values from 6.44°C at 31 mbsf to 7.91°C at 86 mbsf and define a thermal gradient of 24.3°C/km. Using a mean thermal conductivity value of 1.31 W/(m·K), the heat flow is estimated as ~33 mW/m<sup>2</sup>.

### Core-log-seismic integration

LWD data acquired during Expedition 372 in Hole U1519A were correlated with core-based observations and physical properties measurements from Holes U1519C–U1519E and with seismic reflection data across the site in the Tuaheni Basin. LWD *P*-wave velocity and density measurements were used to develop a synthetic seismic trace to correlate the LWD, core, and seismic data (Figure F11), which allowed us to assess the match between the seismic traces that would be predicted from the physical properties in the boreholes with seismic sections acquired across Site U1519 prior to the expedition. Based on the new seismic tie, we defined three major seismic units and compared them with LWD data from Expedition 372 and lithostratigraphic units from Expedition 375.

The upper seismic unit is 281 m thick and comprises a horizontally layered basin-fill sequence, including at least two interpreted MTDs in the upper 141 m and a thick underlying section of inferred highly reflective, presumably sandy, sediments that were not cored. Cores from recovered intervals in this seismic unit comprise mudstones with minor sand and volcanic ash that are younger than 0.53 Ma in age. Both observatory screens were deployed in silty mudstone intervals in this unit. The middle seismic unit is a seaward-dipping 265 m thick slope sequence partially buried by the upper seismic unit. This interval includes a mixture of layered sediments and MTDs interpreted in the seismic data. Only the upper 3.5 m and lower 27 m of this sequence were cored, and these intervals consist of predominantly fine grained mudstone. The lower seismic unit is a strongly reflective interval that dips landward, likely as a result of uplift and tilting by thrust faulting. Cores recovered from this unit to 635 mbsf consist of mudstone and MTDs containing coarser material, which have been dated at 0.54–1.73 Ma, which is younger than the expected Miocene/Pliocene age that was inferred prior to drilling.

## Site U1520

### Background and objectives

The primary objective at Site U1520 was to log and sample the sedimentary sequence on the subducting Pacific plate to provide insight into the lithologies and conditions expected deeper along the subduction interface and in the SSE source area. The site lies ~95 km from shore and 16 km east of the deformation front at ~3520 m water depth (Figures F2, F3; Table T1) (see the [Site U1520](#) chapter [Barnes et al., 2019c]). Site U1520 was expected to encounter sediments and rocks of late Quaternary to Cretaceous age based on regional seismic stratigraphic interpretation of the Hikurangi Plateau and Hikurangi Trough stratigraphy (Figure F2) (Barnes et al., 2010; Davy et al., 2008). The upper ~610–640 m of the section was expected to consist mainly of mud and sand turbidites, hemipelagic sediment, debris flow material, and minor ash of predominantly Pliocene–Quaternary age. The package from ~640 to ~840 mbsf was expected to comprise Late Cretaceous, Paleogene, and Miocene sedimentary rocks of the Hikurangi Plateau cover sequence, including nannofossil chalk, mudstone, tephra, and sandstone with possible unconformities. The strongly reflective sequence deeper than 840 mbsf was interpreted to include basalts, volcanoclastic sedi-

ments, and breccia along with intervals of pelagic chert and/or limestone (e.g., Davy et al., 2008).

The highest priorities at Site U1520 were to measure and recover the materials deeper than ~600 mbsf that represent the protolith for material transported into the SSE source region. Time constraints during Expedition 372 limited drilling with LWD to 750 mbsf at this site, which was short of the planned target of 1200 mbsf. To maximize our ability to sample the deep portion of the section during Expedition 375, we drilled in casing to 642 mbsf in Hole U1520C and conducted RCB coring below the casing to 1054.1 mbsf. Following coring, we conducted wireline logging in the open hole below the casing from 642 to 947 mbsf. We returned to Site U1520 later during the expedition to conduct APC/XCB coring in Hole U1520D to sample the upper 642 m of the section.

The scientific objectives of coring and logging at Site U1520 were to define the structures and deformation, physical properties, lithology and composition, and interstitial fluid geochemistry of the incoming material prior to subduction. These data will also be used for core-log-seismic integration across the Hikurangi Trough. Priorities for post-expedition analysis include but are not limited to measurement of the mechanical, elastic, frictional, and hydrological properties of the incoming sediment and basement along with detailed compositional analyses.

### Expedition 372 operations

#### Transit to Site U1520

The vessel arrived at Site U1520 (proposed Site HSM-05A [Saffer et al., 2017]) at 1302 h (UTC + 13 h) on 26 December 2017 after a 28 nmi transit from Site U1519.

#### Hole U1520A

The LWD BHA was made up with the geoVISION, NeoScope, TeleScope, SonicScope, and proVISION tools. Hole U1520A (38°58.1641'S, 179°7.9357'E; 3521.3 mbsf) was spudded at 0845 h on 27 December 2017. LWD data were collected from 0 to 97.9 mbsf with continuous safety monitoring. Operations in Hole U1520A were terminated early because of deteriorating weather conditions.

#### Hole U1520B

After waiting on weather for 45.75 h (1.91 days), Hole U1520B (38°58.1587'S, 179°7.9233'E; 3520.1 mbsf) was spudded at 1245 h on 29 December 2017. LWD measurements were collected from 0 to 750 mbsf with continuous safety monitoring.

### Expedition 375 operations

#### Transit to Site U1520

We first occupied Site U1520 while waiting for *Tangaroa* to deliver replacement seals needed for the observatory installation at Site U1518. We arrived at Site U1520 at 0257 h (UTC + 12 h) on 28 March 2018.

#### Hole U1520C

First, we fabricated the base of the reentry cone, assembled the hydraulic release tool (HRT) needed to deploy the reentry system, assembled a casing string consisting of 54 joints of 10¾ inch casing and a casing shoe, and secured the casing string in the moonpool at 0130 h on 29 March 2018. Next, we put together the drilling assembly needed to drill in the reentry system. The drilling assembly was composed of a 9¾ inch drill bit, an underreamer with its arms set to 14¾ inches, and a mud motor to rotate the bit and underreamer in isolation from the casing. The underreamer arms were tested, and the drilling assembly was completed and landed inside the casing at

0500 h on 29 March. The drilling assembly and HRT were connected to the casing and mud skirt, the reentry cone was assembled in the moonpool, and the reentry system was lowered to the seafloor. While the reentry system was being lowered to the seafloor, *Tangaroa* arrived at 1615 h to deliver the replacement seals needed for the CORK-II installation at Site U1518.

The subsea camera was deployed to monitor the reentry cone and base while drilling it into the seafloor. Hole U1520C (38°58.1532'S, 179°7.9112'E; 3522.1 mbsl) was spudded at 1940 h on 29 March, and it took ~27 h for the bit to reach a total depth of 646 mbsf with the casing shoe at 642 mbsf. Once the drilling system was released from the reentry system, we recovered the subsea camera and then the drill string at 1120 h. With the reentry system completed, we departed for Site U1518 at 1310 h on 31 March to complete the observatory installation there.

We returned to Site U1520 on 2 April following a ~10 h deviation to the Gisborne Pilot Station for a personnel transfer and reached Hole U1520C at 1848 h on 2 April. We assembled an RCB coring assembly and reentered Hole U1520C at 0525 h on 3 April. The next several hours were spent cleaning cuttings out of the inside of the 642 m deep casing. RCB coring started at 1200 h on 3 April. Cores 2R–44R penetrated from 646.0 to 1054.1 mbsf and recovered 235.81 m (58%). Nonmagnetic core barrels were used for all cores. Coring was terminated so that Hole U1520C could be logged before the weather deteriorated.

To prepare Hole U1520C for logging, we circulated the cuttings out of the hole with mud and recovered the RCB BHA. The subsea camera was deployed to check the reentry cone, which appeared to have sediment inside, and the cone was flushed with seawater. Once the drill string was recovered, we made up a logging BHA and lowered it to the seafloor. Hole U1520C was reentered at 0250 h on 9 April, and the drill pipe was set at 599 mbsf for logging, 42 m above the casing shoe. We deployed a modified triple combo tool string with the following tools (from the bottom up):

- Dipole Shear Sonic Imager (DSI; sonic velocity),
- High-Resolution Laterolog Array (HRLA; resistivity),
- Hostile Environment Litho-Density Sonde (HLDS; caliper only, without the density source), and
- Enhanced Digital Telemetry Cartridge (EDTC; gamma ray and telemetry).

We made two logging passes from 642 to 947 mbsf where we encountered an obstruction 107 m from the bottom of the hole. The tools were back on the rig floor at 1505 h on 9 April, and the drill string was recovered at 0010 h on 10 April, ending operations in Hole U1520C. The next objective for the expedition was to install an observatory at Site U1519 and core at Site U1526.

#### Hole U1520D

After a ~6 h transit from Site U1526, we arrived at the specified coordinates of Hole U1520D at 2305 h on 24 April 2018. Our objective for Hole U1520D was to core the uppermost sediment (shallower than 646 mbsf) that we drilled without coring in Hole U1520C. After assembling an APC/XCB BHA, Hole U1520D (38°58.1475'S, 179°7.8991'E; 3520.3 mbsl) was spudded at 0850 h on 25 April. Cores 1H–67X advanced from 0 to 642.3 mbsf and recovered 318.38 m (62%). In this interval, we drilled without coring from 189.3 to 220.0 mbsf and from 270.8 to 366.6 mbsf. Coring was suspended from 1600 h on 29 April to 1315 h on 30 April while we waited on weather. Nonmagnetic core barrels were used with all APC cores. Formation temperature measurements were taken with

the APCT-3 for Cores 4H, 7H, 10H, 13H, 16H, 19F, 23F, and 27F. The time spent at Site U1520 during Expedition 375 was 18.26 days. The total time spent at Site U1520 during both expeditions was 21.16 days.

## Principal results

### Logging while drilling

Six LWD tools (NeoScope, SonicScope, TeleScope, proVISION, geoVISION, and StethoScope) were deployed in Holes U1520A and U1520B, providing both real-time and recorded-mode data (Table T1). In both holes, the resistivity image quality is degraded because of tool stick and slip caused by the high drilling penetration rate.

References to major reflection units determined from seismic sections were used to help define logging units in the sedimentary section. Nine logging units were identified in Hole U1520B, reflecting significant changes in the sediment physical properties recorded by the logs (Figure F12). The uppermost 100 m is interpreted to be relatively sandy sediment, mainly turbidities, associated with borehole washouts. These overlie ~110 m of finer grained sediments of what is interpreted to be the Ruatoria MTD. The sediments beneath the Ruatoria MTD comprise alternating fine- and coarser grained sedimentary packages that show progressively increasing density and decreasing porosity with depth to a boundary at ~510 mbsf. At this depth, a marked change to sediments with a different acoustic character, higher density, and significantly lower gamma ray signature is evident. Several units with distinct logging characteristics are identified in the lower 150 m of the borehole. Although the logs do not enable direct identification of the rock type, the petrophysical characteristics and the tie to seismic reflectivity indicate that the drilled section corresponds to the pelagic sequence overlying the Hikurangi Plateau. Owing to generally poor hole conditions and a fast rate of penetration, the image logs are poor quality through much of the drilled section in both Holes U1520A and U1520B. Dipping beds, however, were identified in many of the logging units. Above ~510 mbsf, bedding dip inclination and azimuth appear to be variable, particularly in the Ruatoria MTD. In the underlying sequence, the bedding dips are most commonly at low angles to the northwest, west, and southwest. Several high-angle resistive fractures were identified in the sediments between 100 and 150 mbsf and between 660 and 710 mbsf in Hole U1520B.

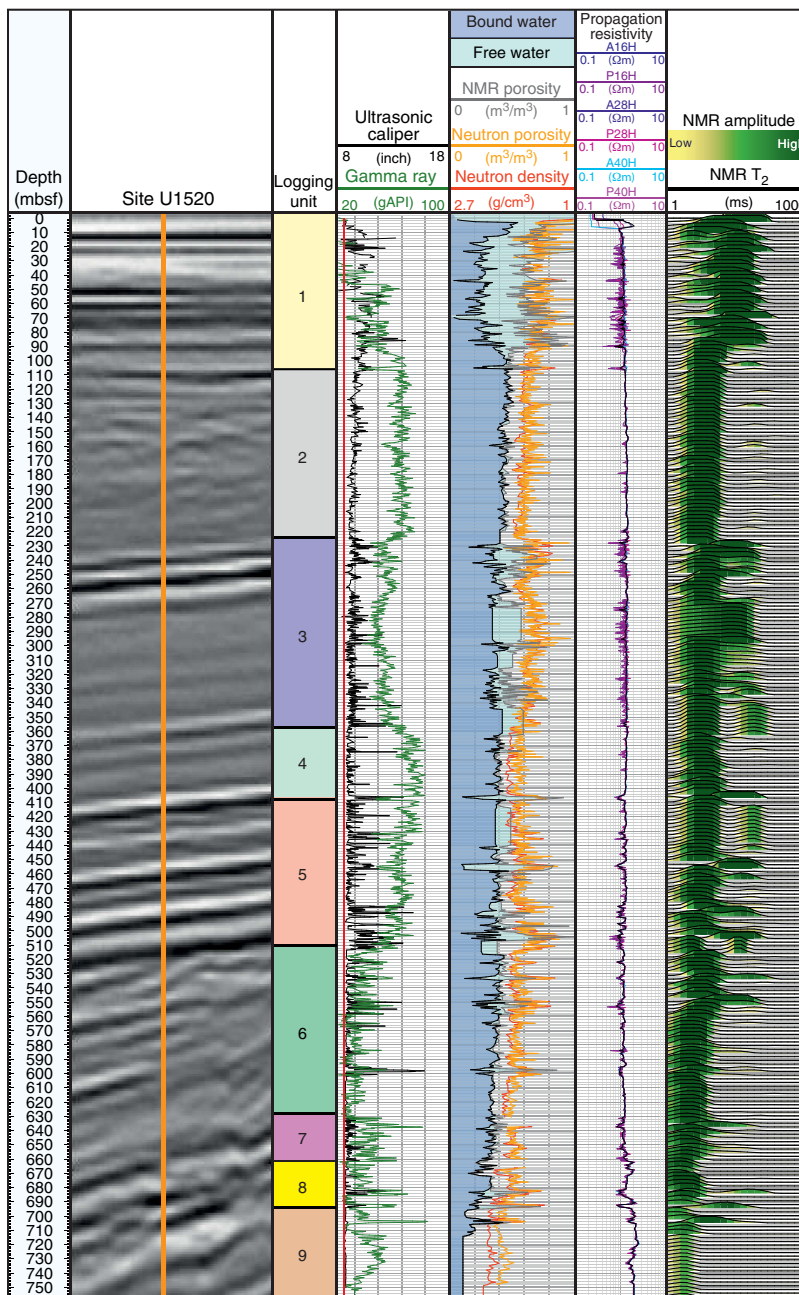
### Lithostratigraphy

Six lithostratigraphic units were defined from cores collected at Site U1520 (Figure F13). The sediments and sedimentary rocks range in age from Cretaceous to Holocene. Thin tephra layers are scattered throughout most of the succession.

Lithostratigraphic Unit I begins at the seafloor and extends to 110.5 mbsf. This interval consists of greenish gray hemipelagic mud punctuated by graded beds of dark gray silt and sand. We interpret the coarser beds to be products of deposition by turbidity currents on the floor of the Hikurangi Trough.

Lithostratigraphic Unit II (110.5–222.0 mbsf) consists of hemipelagic mud with silt interbeds. These turbidites are generally finer grained and thinner than those recovered in Unit I. Based on interpretations of seismic reflection data, Unit II is thought to represent the distal edges of the Ruatoria debris avalanche. However, mesoscopic evidence is lacking for the types of soft-sediment, gravity-driven deformation expected in a submarine slide or debris flow deposit (e.g., truncated and rotated laminae, irregular bedding dips, fragmentation of cohesive mud clasts, clasts-in-matrix fabrics, and flow banding).

Figure F12. Composite plot of seismic image (Profile 05CM-04) and selected LWD measurements, Site U1520. PSDM from Barker et al. (2018).



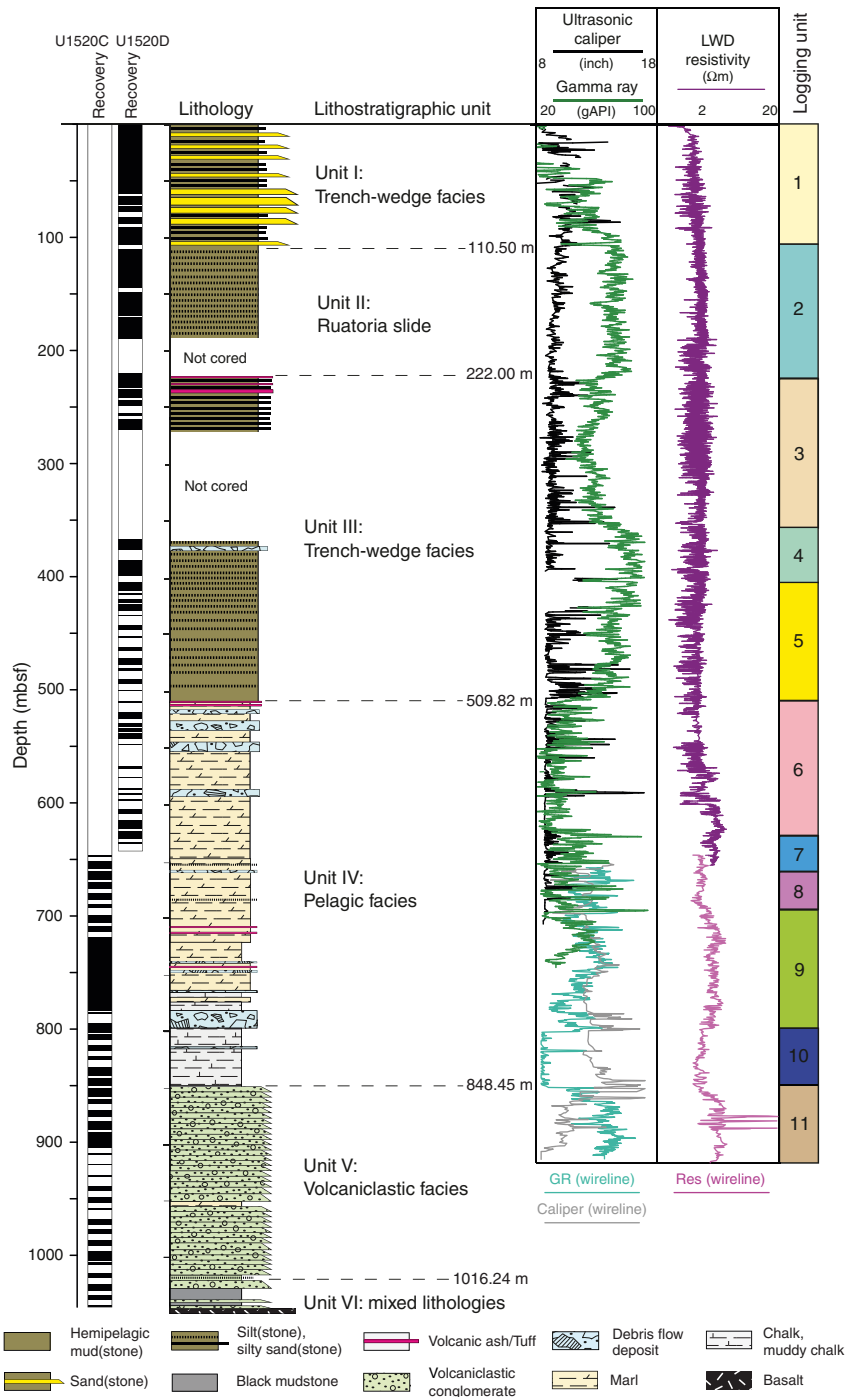
Lithostratigraphic Unit III (222.0–509.82 mbsf) is similar to Unit I but without thick sand beds. The turbidites are characterized by graded beds of fine sand to silt with planar- and cross-laminae. We interpret the depositional environment to be in the Hikurangi Trough during a period of time in which turbidity currents were less frequent, more dilute, and finer in grain size.

Lithostratigraphic Unit IV begins at 509.82 mbsf in Hole U1520D and extends to 848.45 mbsf in Hole U1520C. Lithologies change markedly across the Unit III/IV boundary to a strongly lithified Pleistocene–Paleocene pelagic carbonate facies that includes light greenish gray marl, light brownish gray calcareous mudstone, and pale brown chalk. Secondary lithologies include matrix-supported gravity-flow deposits and volcanic tuff. The debris flow de-

posits display contorted to fragmented marl and chalk, together with angular to subrounded clasts of volcanoclastic sandstone and vesicular basalt.

Lithostratigraphic Unit V (848.45–1016.24 mbsf) is dominated by heavily altered, granule-sized volcanoclastic conglomerate. These Cretaceous deposits are characterized by subangular clasts of basalt that range in size from a few millimeters to 6 cm. The fabric ranges from clay matrix supported to clast supported, and the mechanisms of emplacement probably included grain flow and debris flow. Alteration of the basalt clasts to palagonite and clay minerals (smectite) is pervasive. Zeolite (phillipsite) and calcite are common cements.

Figure F13. Stratigraphic column, Holes U1520C and U1520D. Gamma ray (GR), caliper, and resistivity (Res) are from LWD data acquired during Expedition 372 and wireline logging data acquired during Expedition 375. Wireline data are shown only for the main pass at depths below the casing shoe at 642 mbsf.

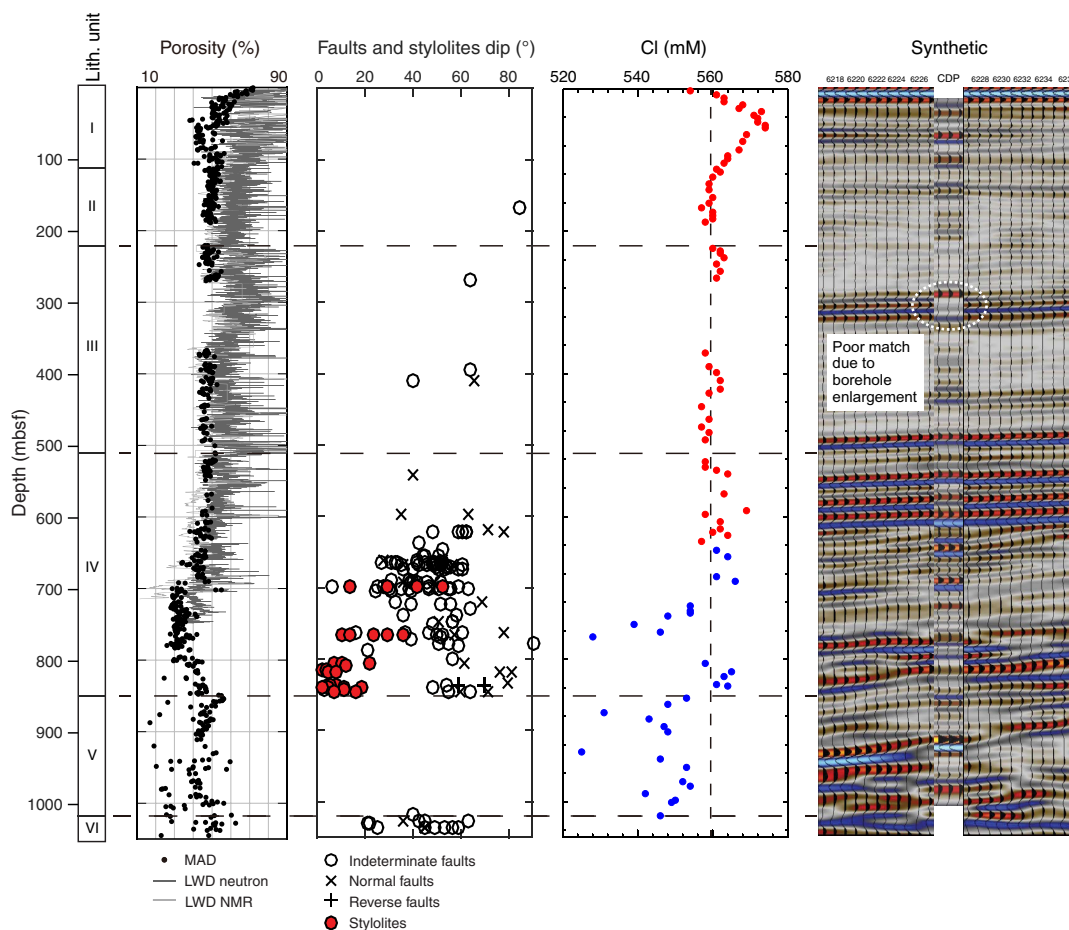


Lithostratigraphic Unit VI (1016.24–1045.75 mbsf) comprises a blend of rock types whose stratigraphic organization and thicknesses are not resolvable. Much of the unit contains alternating volcaniclastic conglomerate and siliceous mudstone with a distinctive dark bluish gray to greenish gray color. Additional lithologies include pyrite-rich siltstone, organic-rich black mudstone, white limestone, reddish brown siltstone, and vesicular basalt with amygdules.

### Biostratigraphy

The sedimentary sequence and upper portion of the Hikurangi Plateau basement cored at Site U1520 represent a discontinuous Holocene to Late Cretaceous succession comprising several hiatus-bounded packages. Planktonic foraminifers and calcareous nannofossils indicate that Holes U1520D and U1520C recovered Holocene sediment (younger than 0.011 Ma) from 0 to 5.88 mbsf, Pleistocene sediment (0.011–2.17 Ma) from 15.40 to 537.11 mbsf,

Figure F14. Selected drilling results and core-log-seismic tie (synthetic seismic trace), Site U1520. Chlorinity: red = Hole U1520D, blue = Hole U1520C, dashed line = seawater concentration.



Pliocene sediment from 543.45 to 577.32 mbsf, a Pliocene/Miocene boundary sequence from 587.74 to 592.94 mbsf, Miocene sediment from 609.71 to 746.82 mbsf, late Oligocene sediment from 756.62 to 766.15 mbsf, middle to early Eocene sediment from 775.17 to 825.47 mbsf, and middle to early Paleocene sediment from 827.04 to 848.01 mbsf.

The underlying volcanoclastic sequence (849.96–1045.75 mbsf) spanning lithostratigraphic Units V and VI is largely unfossiliferous, except for 950.22–953.45 and 1016.69–1017.82 mbsf, where Late Cretaceous foraminifers were recovered. Organic-rich sediments from 1036.57 to 1037.17 mbsf also include poorly preserved radiolarian faunas and siliceous branching tube-like fossils of unknown affinity. Minor reworking of planktonic foraminifers is evident throughout the cored sedimentary succession but is most notable at ~512 mbsf, where common, well-preserved middle to early Eocene, Miocene, and Pliocene taxa are present in a Pleistocene fauna, and at ~588 mbsf, where late Miocene (8.96–9.63 Ma) taxa dominate a Miocene/Pliocene boundary fauna.

#### Paleomagnetism

Paleomagnetic investigations included NRM measurement of archive halves prior to and following stepwise AF demagnetization to peak fields of 30 or 40 mT. In addition, 1–2 discrete samples per core were subjected to more detailed AF or thermal demagnetization. The data quality and processing strategy differed somewhat for

Holes U1520C and U1520D as a result of the different coring systems used, core disturbance, and recovery. With few exceptions, characteristic remanent magnetization directions calculated from data sets based on discrete samples were mostly coherent. A magnetostratigraphy was produced with confidence for APC and RCB cores (375-U1520D-1H through 30H and 375-U1520C-2R through Section 23R-6) and tentatively for XCB cores (375-U1520D-31X through 66X). The volcanoclastic deposits of Lithostratigraphic Units V and VI all yield steep negative inclinations, suggesting that the entire unit may have been remagnetized. The Brunhes/Matuyama Chron boundary was identified at 413 mbsf, which is roughly consistent with biostratigraphic ages. Additional polarity horizons will be identified post-expedition.

#### Structural geology

The sediments encountered at Site U1520 are generally undeformed. Bedding dips gently ( $<30^\circ$ ) over the entire depth of the hole, with the exception of folded strata in debris flow deposits. The resistivity image log shows some intervals of steeper dips that are not recognized in the cores. Discrete small displacement deformation features were observed throughout Hole U1520C (646–1036 mbsf) but are largely absent shallower than 596.4 mbsf in Hole U1520D (Figure F14).

Distinct structural domains are broadly correlated with lithostratigraphic units. Domain 1 (0–596.4 mbsf) is defined by sub-



horizontal to gently dipping beds with no discrete deformation features. Several high-angle resistive fractures were identified in LWD image logs between 100 and 150 mbsf. Deeper than 596.4 mbsf, faults (normal when sense of slip was determined) and dissolution features are present throughout Domain 2 (596.4–848.45 mbsf), which consists of calcareous clay-rich sediments (Figure F14). These observations are consistent with high-angle resistive fractures documented in LWD image logs between 660 and 710 mbsf in Hole U1520B. Domain 3 is characterized by veins that are common in the variably cemented volcanoclastic sediments that make up this interval (848.45–1016.24 mbsf). Domain 4 (1016.24–1045.75 mbsf) coincides with Lithostratigraphic Unit VI, where deformation structures include several minor faults and few scattered veins.

### Geochemistry

In total, 89 WR samples were collected and squeezed for shipboard and shore-based pore water chemical analyses. Despite the high bulk density and cemented nature of the sediments recovered from Hole U1520C, pore water was recovered from all three lithostratigraphic units. The geochemical profiles at Site U1520 are complex and likely reflect the combined effects of organic matter diagenesis, nonsteady-state sedimentation, volcanic ash/silicate mineral diagenesis, carbonate mineral diagenesis, solute diffusion, and potential lateral fluid flow in the volcanoclastic sediments of Lithostratigraphic Unit V.

Chloride concentrations increase linearly to a peak at 51.3 mbsf (Figure F14), decrease to 142 mbsf, and remain relatively constant to the base of Lithostratigraphic Unit III. Collectively, these profiles suggest a zone of localized volcanic ash alteration/silicate mineral diagenesis and the precipitation of hydrous aluminosilicate minerals in Unit I. Below this zone, in the lower portion of Unit IV and in Unit V, Cl concentrations are depleted relative to seawater and marked by several local excursions to lower values over intervals of ~10 m to a few tens of meters in thickness, which may reflect introduction of freshened water at these depths.

Contemporary carbonate mineral recrystallization is manifested by elevated dissolved Sr concentration in Lithostratigraphic Unit IV shallower than 769 mbsf. Deeper than 769 mbsf, Sr concentration decreases monotonically to near constant values in Unit V. The decrease in Sr concentration at the base of Unit IV suggests that carbonate recrystallization is minor and that present-day carbonate diagenesis is restricted to the top of Unit IV. Sulfate concentration increases linearly through the lower part of Unit IV and remains elevated and nearly constant in Unit V. A similar pattern occurs in the Sr and Mg profiles. Maintaining this gradient likely requires introduction of a sulfate-enriched fluid in the volcanoclastic sediments, likely caused by lateral fluid flow and perhaps in a manner similar to off-axis hydrothermal flow systems in igneous ocean crust (i.e., Baker et al., 1989; Fisher and Wheat, 2010; Solomon and Kastner, 2012; Vannucchi et al., 2013). A total of 93 samples from Hole U1520C and 108 samples from Hole U1520D were taken for carbonate analyses. In Units I–III, CaCO<sub>3</sub> content varies from 2.06 to 18.4 wt%. In Units IV–VI, CaCO<sub>3</sub> content varies from 0.35 to 96.9 wt%, reflecting variations in lithology. The CaCO<sub>3</sub> profile mimics the total carbon and inorganic carbon profiles, with similar trends in all lithostratigraphic units. In the deepest part of Unit IV, CaCO<sub>3</sub> content ranges from 90.0 wt% at 799.0 mbsf to 91.4 wt% at 844 mbsf. This high carbonate abundance reflects the presence of pelagic carbonate. In Unit V, peaks in CaCO<sub>3</sub> content generally reflect local-

ized calcite cement. Organic carbon values are generally low (<1.19 wt%) throughout the section.

### Physical properties

Porosity decreases with depth from 72% at the seafloor to 28%–38% at ~800 mbsf, with some lower values of ~40% between 40 and 106 mbsf that correspond to sand layers. Deeper than 800 mbsf, porosity increases to 56%. Deeper than 855 mbsf, porosity generally decreases with depth but with substantial scatter to the bottom of the hole; the lowest porosities in this interval (Lithostratigraphic Units V and VI) correspond to local (centimeter to tens of centimeters thick) zones of enhanced carbonate and zeolite cementation. The scatter is associated with varying degrees of cementation (Figure F14). Porosity measured on cores is in good agreement with LWD density and porosity values.

*P*-wave velocity ranges from 1450 to 1800 m/s between the seafloor and ~90 mbsf. Between 90 and 420 mbsf, *P*-wave velocity measurement was mostly unsuccessful because of gaps between cores and liners and expansion cracks. Between 420 and ~845 mbsf, velocity generally increases with depth, ranging from 1500 to 2700 m/s, with little scatter. Deeper than 845 mbsf in volcanoclastic Lithostratigraphic Units V and VI, *P*-wave velocity exhibits significant scatter, ranging from 1800 to ~5000 m/s. Undrained shear strength increases with depth from 0–10 kPa at the seafloor to 100–150 kPa at 150 mbsf and remains constant to 400 mbsf followed by a rapid increase with depth to ~600 kPa at 500 mbsf.

NGR ranges from ~0 to 75 counts/s. Mean values are between 30 and 50 counts/s in all units, except lithostratigraphic Unit IV, where the mean NGR value is ~20 counts/s. Magnetic susceptibility is nearly constant with depth in Units I–III and ranges from  $20 \times 10^{-5}$  to  $40 \times 10^{-5}$  SI. In Unit IV, magnetic susceptibility increases with depth from  $10 \times 10^{-5}$  at ~510 mbsf to  $100 \times 10^{-5}$  at ~700 mbsf and then decreases to  $\sim 4 \times 10^{-5}$  SI at 800–849 mbsf. At the top of Unit V at ~849 mbsf, magnetic susceptibility shifts rapidly to  $100 \times 10^{-5}$  SI and then gradually increases with depth to  $300 \times 10^{-5}$  SI at ~900 mbsf, followed by a gradual decrease with depth to  $10 \times 10^{-5}$  SI at ~1020 mbsf. At 1045 mbsf, magnetic susceptibility rapidly increases to  $\sim 300 \times 10^{-5}$  SI.

Thermal conductivity increases with depth from 1.0 W/(m·K) at the seafloor to 1.3 W/(m·K) at ~20 mbsf and remains nearly constant to ~550 mbsf. Some higher thermal conductivity values of 1.6–1.9 W/(m·K) occur between 23 and 87 mbsf and correspond to sand layers. Measurements were not made between 550 and 646 mbsf because the sediments were too indurated for a needle probe and too fragile and disturbed by coring for the half-space probe. Thermal conductivity increases from ~1.2 W/(m·K) at 648 mbsf to 1.8 W/(m·K) at 700 mbsf and then remains relatively constant to ~850 mbsf. Deeper than 850 mbsf, thermal conductivity is nearly constant, with an average of 1.2 W/(m·K).

### Downhole measurements

Five APCT-3 formation temperature measurements were combined with thermal conductivity measurements and yielded a heat flow of 44 mW/m<sup>2</sup> and a temperature gradient of 38°C/km. This heat flow value is consistent with heat flow measurements made using a 3.5 m thermal probe during the R/V *Roger Revelle* Cruise RR1508 in the same location (Harris et al., 2016).

Hole U1520C was logged using a modified triple combo tool string that included borehole diameter from a mechanical caliper (HLDS), gamma ray (EDTC-B), resistivity (HRLA), and DSI. The

nuclear source was not mounted on the HLDS. Although some differences exist, wireline logs are generally consistent with LWD data collected during Expedition 372 (Figure F13) (see **Downhole measurements** in the Site U1520 chapter [Barnes et al., 2019c]). The caliper shows that the hole ranges in size from 8 inches (likely caused by collapse or swelling of clays) to 17 inches. The hole is irregular with many washouts deeper than 780 mbsf. In the uncased portion of Hole U1520C, gamma ray varies between ~20 and 80 gAPI, *P*-wave velocity varies between ~1.6 and 2.9 km/s, and resistivity is relatively constant at ~2 Ωm, with the exception of strong peaks between 870 and 890 mbsf. In general, gamma ray and *P*-wave velocity are inversely correlated between 640 and 848 mbsf and positively correlated deeper than 848 mbsf. Deeper than 848 mbsf, in Lithostratigraphic Units V and VI, *P*-wave velocity, resistivity, and gamma ray all exhibit large variations over short (approximately meter scale) distances, similar to variations in core-based measurements, but are likely muted because of smoothing associated with the large measurement interval for the logs relative to that for discrete core samples.

#### Core-log-seismic integration

The *P*-wave velocity data from LWD and wireline logging were integrated to develop a velocity model to 944 mbsf. Because density data were not recorded during Expedition 375 wireline logging, the density data from LWD were merged with whole-round track and discrete sample data to construct a density model. A synthetic seismic reflection trace was developed to tie the LWD, core, and seismic data (Figure F14). Considering the new seismic tie from this analysis, we defined nine seismic units and compared them with LWD data from Expedition 372 and wireline data and lithostratigraphic units from Expedition 375.

Seismic Unit 1 is 106 m thick and comprises moderate- to low-amplitude, laterally continuous reflections. Cores show the sequence to comprise mud, silt and fine-grained sandy turbidites, and hemipelagic sediments of Late Pleistocene to Holocene age. Unit 2 is 119 m thick and is characterized by moderate- to low-amplitude, semicontinuous and chaotic reflections interpreted from seismic and LWD data to represent the Ruatoria avalanche MTD. In Hole U1520D, cores were only recovered from the upper 80 m of the unit, and the base of the unit was not recovered. The lithofacies is composed mostly of interbeds of hemipelagic mud and thin horizontal silty turbidites with scattered mud intraclasts and erosional bases. The sequence appears largely undisturbed. Units 3–5 consist of variable amplitude, laterally continuous reflections that can be traced widely along and across the Hikurangi Trough. Coring reveals that these units are composed of normally graded silty turbidites with thick volcanic ash layers near the top of the unit. Microfossil ages indicate that these are early to Late Pleistocene in age.

Seismic Units 6–8 have more irregular geometry than the overlying units and moderate- to low-amplitude reflections locally offset by small normal faults. The disrupted nature of the reflections in Unit 6 could be interpreted to be one or more debris flows originating from the flanks of Tūranganui Knoll. Coring reveals that these units are composed of marl and calcareous mudstone with tuff and thin MTDs overlying chalk. Biostratigraphy indicates that these units are early Paleocene to early–Middle Pleistocene in age. Unit 9 consists of high-amplitude reflections that are semicontinuous to discontinuous and corresponds to Lithostratigraphic Units V and VI, which are composed predominantly of mixed, variably cemented volcanoclastic lithologies, thin intervals of calcareous, siliceous, and organic-rich mudstone, and basalt. The seismic units

exhibit overall progradational geometry toward the west, building outward into the basin away from the flank of Tūranganui Knoll. Microfossil ages indicate that Unit 9 is late Early Cretaceous to Late Cretaceous in age.

## Site U1526

### Background and objectives

The primary drilling objective at Site U1526 was to sample the thin sediment cover (~30 m) and ~100–150 m of underlying volcanoclastics or basement on the western flank of Tūranganui Knoll seamount at 2908 m water depth (Figures F2, F3; Table T1) (see the **Site U1526** chapter [Wallace et al., 2019]). The scientific aim of coring was to characterize the seamount's composition, physical properties, extent of alteration and hydration, and structure and hydrogeology prior to transport into the SSE source region. Seismic imaging shows that subducted seamounts present in the source region of shallow SSEs along the drilling transect (Bell et al., 2010) are possible barriers to SSE propagation (Wallace et al., 2016; Figure F1) and that they may potentially be related to the location of historical tsunami earthquakes (Bell et al., 2014). Priorities for post-expedition core analysis include but are not limited to measurement of the mechanical, elastic, frictional, and hydrological properties of the incoming sediment and basement along with detailed analyses of composition and alteration.

### Operations

#### Transit to Site U1526

The vessel arrived at Site U1526 (proposed Site HSM-08A [Saffer et al., 2017]) at 1700 h (UTC + 12) on 22 April 2018.

#### Hole U1526A

An RCB BHA was assembled, and the drill string was lowered to the seafloor. Hole U1526A (39°1.3203'S, 179°14.7594'E; 2890.1 mbsl) was spudded at 0150 h on 23 April 2018. Cores 1R–14R advanced from 0 to 83.6 mbsf and recovered 29.26 m (35% recovery). Nonmagnetic core barrels were used for all RCB cores. At the completion of coring, the drill bit was partially raised from the seafloor, and the ship returned to nearby Site U1520.

#### Hole U1526B

On 2 May 2018, we returned to Site U1526 following an 8 h transit from Site U1520 in dynamic positioning mode. The ship was offset 20 m west-northwest from Hole U1526A, and Hole U1526B (39°1.3146'S, 179°14.7481'E; 2888.4 mbsl) was spudded at 2015 h on 2 May. APC Cores 1H–4H and XCB Core 5X advanced from 0 to 33.5 mbsf and recovered 31.56 m (94%). Nonmagnetic core barrels were used for all APC cores. The time spent at Site U1526 was 2.88 days.

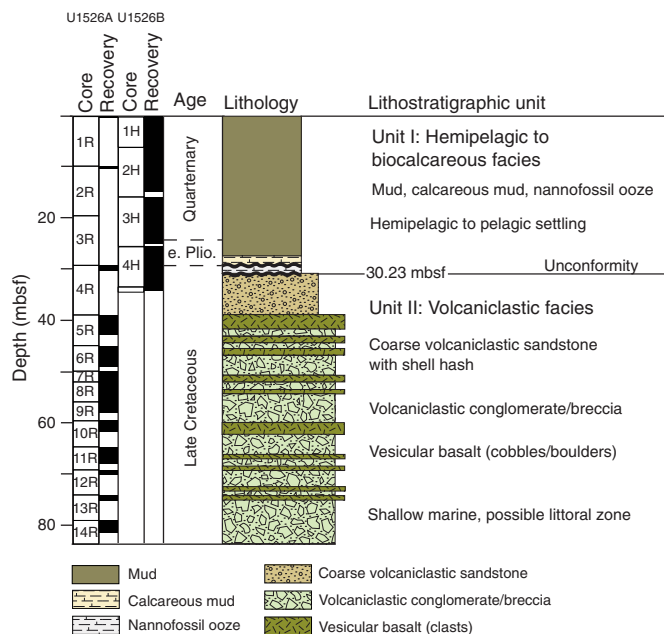
The *JOIDES Resolution* started the transit to Auckland, New Zealand, at 1200 h on 3 May. Expedition 375 ended with the first line ashore at the Freyberg Wharf in Auckland at 0652 h on 5 May.

### Principal results

#### Lithostratigraphy

We identified two lithostratigraphic units at Site U1526 (Figure F15). Lithostratigraphic Unit I is a highly condensed section characterized by fine-grained, mixed (i.e., siliciclastic–calcareous) and biocalcareous sediment. Carbonate content increases progressively downsection. Unit I extends from 0 to 30.23 mbsf and is composed of mud, calcareous mud, and nannofossil-rich ooze. The greenish gray mud contains foraminifer-rich silt and ash layers. Between 26.91 and 30.23 mbsf, the lithology changes to light green calcareous

Figure F15. Stratigraphic column, Holes U1526A and U1526B.



ous mud with nannofossils and, across a significant unconformity, to pale brown nannofossil ooze. Unit I ranges in age from Holocene to Late Cretaceous.

The Lithostratigraphic Unit I/II boundary at 30.23 mbsf is characterized by a 20 cm thick interval rich in manganese concretions. Unit II is Late Cretaceous in age and dominated by volcaniclastic conglomerate with variably altered basalt clasts in a sand-sized matrix composed of shell and basalt fragments (Figure F15). The top of the volcaniclastic conglomerate is characterized by abundant intact shells. Because of the sharp contact between the dramatically different lithofacies and the presence of the manganese crust at the top of Unit II, we interpret the unit boundary to be an unconformity. Basalt clasts generally range from centimeter to decimeter scale, with some intervals extending for 1–2 m. The extent of basalt alteration is highly variable, and many samples show good preservation of plagioclase and clinopyroxene.

#### Biostratigraphy

The sedimentary succession cored at Site U1526 ranges in age from Holocene to Late Cretaceous (Figure F15). High foraminiferal and nannofossil abundances with moderate to very good preservation were observed throughout the hemipelagic sedimentary cover (Lithostratigraphic Unit I). Below this interval, in Unit II, volcaniclastic coarse sandstones and conglomerates are barren of microfossils, although macroinvertebrate remains allow for broad biostratigraphic constraint and paleowater depth reconstruction.

Planktonic foraminifers and calcareous nannofossils indicate that Hole U1526A recovered a succession of Holocene to Middle Pleistocene (0–0.63 Ma) sediments from 0.0 to 19.94 mbsf that overly early Pliocene (4.57–5.15 Ma) sediments from 20.46 to 21.04 mbsf. The underlying volcaniclastic section recovered in Hole U1526A (29.1–81.39 mbsf) is generally barren of microfossil remains; however, a coarse sand-sized volcaniclastic sandstone to conglomerate in the upper portion (29.1–38.8 mbsf) of Lithostratigraphic Unit II contains abundant bivalve shells. Below this interval, large subrounded to subangular pebbles and boulders of variably al-

tered to fresh basalt are embedded in a coarse volcaniclastic sand matrix that contains remobilized shell material, echinoid spines, and coralline algae. Planktonic foraminifers and calcareous nannofossils indicate that Hole U1526B recovered Holocene (younger than 0.011 Ma) sediments from 0 to 0.06 mbsf, Middle to early Pleistocene (0.53–2.17 Ma) sediments from 5.7 to 24.09 mbsf, and Late Cretaceous (~66–74 Ma) sediments at 30.20 mbsf.

Planktonic foraminifer abundances and benthic foraminifer assemblages throughout Lithostratigraphic Unit I are indicative of open oceanic settings and mid- to lower bathyal water depths (>600 m), respectively. Macroinvertebrate remains in Unit II are consistent with Late Cretaceous shallow-water bioclastic material transported downslope.

#### Paleomagnetism

Paleomagnetic investigations at Site U1526 focused on producing a preliminary magnetostratigraphy for the sedimentary cover sequence sampled in Hole U1526B, resolving remanence intensity and demagnetization behavior of volcaniclastic material recovered deeper than 24 mbsf, providing constraints on the emplacement temperatures of the volcaniclastic material, and exploring the possibility that in situ lava flows are present. Analyses included continuous NRM measurement of archive halves prior to and following AF demagnetization. An additional 14 discrete samples from individual basaltic clasts were subjected to thermal demagnetization experiments.

The pelagic sediments in Hole U1526B yield NRMs in the range of ~0.005 to 0.5 A/m that decay rapidly during removal of a steep drilling overprint. Following AF treatment to 10 or 20 mT, inclination records display a well-defined pattern with multiple switches from negative (normal polarity) to positive (reversed polarity) inclinations with sharp transitions.

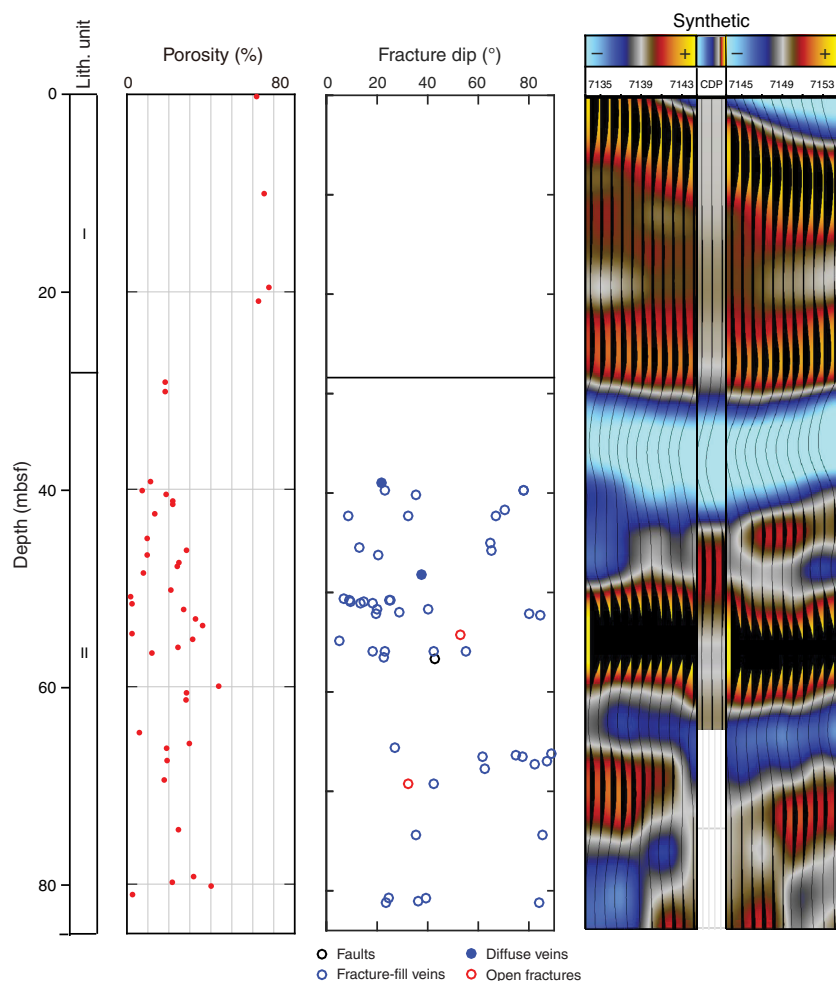
The NRM of the volcaniclastic materials in Lithostratigraphic Unit II ranges from ~0.2 to 13.0 A/m. The NRM directions have inclinations that usually differ among mafic clasts, suggesting that the clastic material was emplaced at ambient (“cold”) temperatures. Remanent magnetization directions from discrete samples are consistent with the directions measured on archive halves. Samples generally yield high-quality demagnetization behavior and primarily demagnetize in the blocking temperature range of 250°–350°C, suggesting that titanomagnetite or titanomaghemite is the main remanence carrier.

Basalts recovered between 57.2 and 64.8 mbsf yield consistent steep and negative NRM inclinations similar to the inclination of a ~1.5 m long and mostly intact piece of basalt recovered between 24.6 and 26.03 mbsf, which raises the possibility that in situ lava flows may be present, although heavily fractured, in the sequence.

#### Structural geology

Bedding planes are difficult to resolve throughout the cored interval at Site U1526, but subhorizontal bedding is recognized in the upper sedimentary veneer. Fractures and veins are the most common structural features (Figure F16), occur in both clasts and matrix, and locally follow clast/matrix boundaries. Some clasts are brecciated, and some are cut by veins that continue into the matrix. Both fracture-filled and diffuse veins are present in the volcaniclastic deposits. We defined two distinct structural domains at this site. Domain 1 contains subhorizontal fine-grained sediments with no veins. Domain 2 contains volcaniclastic sediments and basalt and is distinguished by varying degrees of cementation and veining.

Figure F16. Selected drilling results and core-seismic tie (synthetic seismic trace), Site U1526.



### Geochemistry

The main objective of the inorganic geochemistry program at Site U1526 was to identify diagenetic reactions and to evaluate the possibility of vertical recharge of seawater through the Tūranganui Knoll seamount. A total of 11 routine pore water WR samples were collected from APC cores in Hole U1526B and squeezed for ship-board and shore-based pore water chemical analyses. The geochemical profiles at Site U1526 reflect the combined effects of early organic matter diagenesis and carbonate/silicate mineral diagenesis. Many solutes exhibit a sharp gradient in their profiles that approaches the volcanoclastic sediments of Lithostratigraphic Unit II to a modified fluid composition similar to that of the volcanoclastic unit (Unit V) at Site U1520.

Hydrocarbon gases were not detected at Site U1526. In Lithostratigraphic Unit I (0–30.23 mbsf), which consists of fine-grained mixed to biocalcareous sediment,  $\text{CaCO}_3$  content exhibits a large degree of scatter (from 1.26 to 69.99 wt%).  $\text{CaCO}_3$  content increases with depth and reaches the highest value (69.99 wt%) in Unit I at 21 mbsf, which corresponds to a nannofossil-rich ooze. In Unit II (30.23–81.39 mbsf), which is composed of coarse volcanoclastic sandstone and volcanoclastic conglomerate,  $\text{CaCO}_3$  content also exhibits a large degree of scatter, ranging from 0.25 to 68.30 wt%. The highest value (68.30 wt%) in Unit II is indicative of bivalve shell and calcite cement incorporation in the shell-rich bed at the top of the

volcanoclastic sequence. Organic carbon content is low in Units I and II (from 0.00 to 0.61 wt%); the highest values occur shallower than 21 mbsf and correspond to calcareous mud. C/N ratios range from 20.89 to 190.91.

### Physical properties

Porosity ranges from 62% to 68% between the seafloor and 21 mbsf in Lithostratigraphic Unit I (Figure F16). Porosity decreases abruptly to 18% at ~30 mbsf at the top of Unit II. From 39 mbsf to the bottom of Hole U1526A in Unit II, porosity values exhibit large scatter (2%–44%) and average 20% with no significant downhole trend. In Unit I (0–30 mbsf),  $P$ -wave velocity ranges from 1450 to 1570 m/s. Deeper than 30 mbsf in Unit II,  $P$ -wave velocity ranges from 1700 to ~6000 m/s; significant scatter arises from the heterogeneous nature of the conglomerates and basalt, due in part to variable degrees of cementation. Thermal conductivity ranges between 1.2 and 1.6 W/(m·K) and has a mean of 1.5 W/(m·K). Undrained shear strength increases with depth, ranging from 0 to ~100 kPa between 0 and 30 mbsf. NGR in Unit I mostly ranges between 20 and 40 counts/s, except for lower values of 2–8 counts/s between 27 and 30 mbsf, where nannofossil-rich ooze is present. NGR in Unit II increases from ~29 counts/s at the top of the unit to ~36 counts/s at ~50 mbsf and then decreases gradually to 27 counts/s at the bottom of the cored interval. Magnetic susceptibility mostly ranges from 10

$\times 10^{-5}$  to  $200 \times 10^{-5}$  SI in Unit I, shallower than  $\sim 30$  mbsf. Deeper than  $\sim 30$  mbsf, magnetic susceptibility ranges from  $\sim 100 \times 10^{-5}$  to  $3000 \times 10^{-5}$  SI, with an average of  $\sim 1400 \times 10^{-5}$  SI.

### Core-seismic integration

Core-based observations and measurements in Holes U1526A and U1526B were integrated with seismic reflection data from Tūranganui Knoll. In the absence of logging data, we used *P*-wave velocity and density data from cores to construct a lithologic model and produce a seismic-well tie (Figure F16). *P*-wave velocity data from the Hole U1526B pelagic sediments indicate that velocity in this interval is low, typically ranging from  $\sim 1500$  to  $1530$  m/s, which is consistent with a strong reflection at the base of Lithostratigraphic Unit I that separates the pelagic sediments from cemented volcanoclastic sandstones below. To depth convert the seismic data below Unit I, we used a mean *P*-wave velocity value of  $3805$  m/s from core data.

Two seismic units were identified at Site U1526. Seismic Unit 1 corresponds to Lithostratigraphic Unit I and is represented by a  $30.2$  m thick weakly reflective interval in Hole U1526B. However, the thickness varies significantly away from the site, reaching  $>140$  m elsewhere on Tūranganui Knoll. Cores show that Unit 1 ( $0$ – $30.2$  mbsf) comprises hemipelagic mud, light greenish gray calcareous mud, and brownish white nanofossil-rich ooze with thin layers of volcanic ash. Unit 2 corresponds to Unit II and represents the lower  $44$  m drilled in Hole U1526A but extends below the depth of drilling. The upper part of the unit is strongly reflective, comprising planar to irregular, discontinuous high-amplitude reflections. Cores show that Unit 2 comprises large, subrounded to subangular pebbles and boulders of variably altered to fresh basalt embedded in a matrix of cemented volcanoclastic sand.

## Observatory installations

Borehole observatories were installed at Sites U1518 and U1519. The observatory at Site U1518 (penetrating the Pāpaku fault) includes three levels of pore pressure monitoring, high-resolution temperature monitoring at 30 separate depths, a fluid flowmeter, and time-series fluid sampling for geochemical analyses (Figure F4). The observatory at Site U1519 is similar in overall design (as described below) but includes only two pore pressure monitoring intervals and temperature monitoring at 15 separate depths, with no fluid sampling (Figure F4). Pore pressure monitoring is conducted through hydraulic tubing that terminates in screens outside of the casing, except in the fault zone interval at Site U1518, where the casing is perforated for geochemical sampling. The fluid sampling is conducted using osmotic pumps connected to sampling coils (Janasch et al., 2004). Temperature monitoring is conducted using autonomous temperature sensors suspended in the interior of the casing and within the OsmoSampler package at Site U1518.

Both observatories consist of an outer  $10\frac{3}{4}$  inch casing string with an ACORK head and a  $4\frac{1}{2}$  inch inner casing string with a CORK-II head placed inside the ACORK (Figure F4). For the fault site, Hole U1518G was predrilled to  $433$  mbsf, and the intention was to lower  $10\frac{3}{4}$  inch casing into the hole escorted by an underreamer, mud motor, and drill bit, with the ACORK head attached to the top of the casing. During reentry, however, unanticipated heave caused the bit to knock the reentry funnel away from Hole U1518G, requiring us to drill in the ACORK and casing at the new location of the funnel and mud skirt (Hole U1518H; drilled to  $426$  mbsf). For the Site U1519 observatory, Hole U1519B was predrilled to  $283$  mbsf,

and the  $10\frac{3}{4}$  inch casing was lowered behind an underreamer, mud motor, and drill bit, with the ACORK head attached to the top of the casing. At both sites, an HRT was used to release the ACORK assembly after it was drilled in.

A flatpack umbilical containing three hydraulic lines ( $\frac{1}{4}$  inch diameter) was strapped to the outside of the  $10\frac{3}{4}$  inch casing as it was assembled and run through the moonpool. These lines terminate in casing screens in the target monitoring intervals at depth and are connected to valves and the pressure sensing unit at the ACORK head. Pressure monitoring at Site U1518 takes place in the hanging wall ( $217.7$  mbsf), fault zone ( $332.1$  mbsf), and footwall ( $393.2$  mbsf) of the Pāpaku fault. Pressure monitoring takes place in two intervals at Site U1519 (at  $124$  and  $264$  mbsf). After the ACORK was seated, the CORK-II was lowered into the inner bore of the  $10\frac{3}{4}$  inch ACORK casing and latched into the ACORK head after lowering and landing the instrument string into the CORK-II.

Temperature sensors were attached to a rope ( $\frac{7}{16}$  inch Spectra line) with sinker bars at various depths to hold the rope taut (Figure F4). A total of 30 temperature sensors were installed at Site U1518, with dense spacing spanning the fault zone and coarser spacing in the hanging wall and footwall. The instrument string at Site U1519 consists of 15 temperature sensors. Both instrument strings were lowered through the drill pipe into the inner bore of the  $4\frac{1}{2}$  inch casing and seated with a landing plug at the CORK-II head. The OsmoSamplers and OsmoFlowmeter were lowered as part of the temperature string at Site U1518 (Figure F4) and were landed in a titanium seat inside the CORK-II casing that was positioned in the fault zone interval. Screened, perforated casing ( $7$  m high) at the fault zone monitoring interval allows flow of formation fluids into the OsmoSampler package that monitors fluid flow rates and continuously samples formation fluid for geochemical characterization.

## Preliminary scientific assessment

All of our primary objectives were successfully achieved during Expeditions 372 and 375:

- Acquiring LWD data to characterize geophysical properties at three sites spanning from the subducting Pacific plate through to the upper slope overlying a region of large slow slip;
- Installing two subseafloor observatories to monitor deformation and characterize changes in thermal, hydrological, and chemical state during multiple SSE cycles; and
- Coring at four sites to characterize the physical conditions and rock properties that underlie SSE occurrence.

Overall, the LWD aims achieved during Expedition 372 were reasonably successful, considering that the expedition lost significant time because of weather events and an operational delay prior to departing Australia that was related to biosecurity requirements in New Zealand waters. Target LWD depths were reached at both Sites U1518 ( $600$  mbsf) and U1519 ( $650$  mbsf; Table T1). At Site U1520 in the Hikurangi Trough, LWD reached  $750$  m of the total planned depth of  $1200$  mbsf.

Because of mostly excellent weather and smooth operations, we were able to complete an ambitious slate of planned drilling activities during Expedition 375, including wireline logging the lower portion of Site U1520. Together, Expeditions 372 and 375 implemented a complex, linked data-sharing and sampling plan that spanned two expeditions, several shore-based investigators, and a high volume of sample requests for mission-critical post-expedition studies of rock properties, composition, structures, and deforma-

tion. This plan was largely successful because of the careful coordination of sample requests and sampling strategies during the several months prior to the two expeditions.

### Logging while drilling

A range of LWD tools were successfully deployed at Sites U1518–U1520 during Expedition 372. These tools included the geoVISION (electrical imaging); the NeoScope (propagation resistivity and neutron porosity); the SonicScope (compressional, shear, and Stoneley wave slowness); the TeleScope (measurement-while-drilling data); and the proVISION Plus (NMR). The LWD data were collected to

- Monitor in real time for gas entering the borehole or formation overpressures,
- Facilitate lithologic interpretation,
- Guide interpretation of faults and fractures,
- Determine the maximum and minimum horizontal stress directions,
- Estimate hydrate saturation,
- Constrain elastic moduli for integration with seismic data, and
- Provide guidance for selection of monitoring intervals for the observatories installed during Expedition 375.

The downhole measurement plan for Expedition 372 also included deployment of the StethoScope tool to determine formation pressure and fluid mobility (a measure of permeability) by inserting a probe into the formation wall at selected depths. This tool had never been deployed by IODP, although a similar wireline measurement was made using the Modular Formation Dynamics Tester during Integrated Ocean Drilling Program Expedition 319 (Expedition 319 Scientists, 2010; Saffer et al., 2013). During Expedition 372, the StethoScope was deployed at Site U1518 six times at two stations but failed to record pressure measurements because of a lack of mud seal at the borehole wall.

We drilled two holes (U1518A and U1518B) through the Pāpaku fault because bad weather interrupted operations in Hole U1518A. Hole U1518B produced excellent quality logging data. We successfully drilled to the target depth of 600 mbsf, and interpretation of the LWD data indicates that we penetrated the fault zone at ~320 mbsf. The logs reveal a sequence above the fault with different physical properties than those below (Figure F6). In addition, changes in seismic reflection character in the drilled interval are correlated with variations in logging parameters with depth. The logging data provide detailed insights into the likely lithologies in the borehole and physical properties that reveal deformation, bedding attitude, stress state, and elastic properties. We successfully identified the distribution and density of fractures visible in borehole images and associated structures that can be inferred from bedding dips. These data will help to constrain kinematic models of thrust and fold development. We also observed borehole breakouts oriented approximately north–south, suggesting an east–west-oriented maximum horizontal stress. Another important success at Site U1518 was the successful collection of continuous high-resolution data to aid in selecting depth targets for the borehole observatory installation during Expedition 375.

The primary objective at Site U1519, in the upper margin slope basin, was to log to 650 mbsf to help characterize the nature of the sedimentary sequences before a planned borehole observatory installation during Expedition 375. We successfully acquired generally high quality logging data to the target depth. We found an excellent

correlation between changes in logging parameters and three major sedimentary sequences that were interpreted on seismic reflection profiles prior to drilling (Figure F9). In addition, a remarkably good match occurs between subunits recognized in the logs and complex subunits that were inferred to correspond to changes in lithology in the seismic data. Shipboard analysis indicates that the logs provide information on bedding thicknesses and dips, fracture orientations, and density. The lower part of the borehole successfully penetrated a westward-dipping sedimentary sequence beneath the seafloor that lies on the landward (back limb) side of an apparently inactive thrust fault. Borehole breakouts in the lower part of the hole are oriented northeast–southwest, suggesting an approximately margin normal–directed maximum horizontal stress. Logging properties, such as compressional and shear wave velocity and density data, will improve analysis of seismic reflection data away from the borehole. Similar to Site U1518, collection of continuous high-resolution data was of great value toward selecting depth targets for the borehole observatory installation at this site.

We drilled two holes (U1520A and U1520B) in the subduction inputs sequence in the Hikurangi Trough because bad weather interrupted operations while drilling Hole U1520A (Table T1). Hole U1520B reached a total depth of 750 mbsf and was then abandoned to undertake other work at Site U1517. Consequently, we did not reach our predrilling objective of drilling through the oldest sedimentary sequences and penetrating the inferred volcanic rocks corresponding to the lower flank of Tūranganui Knoll. Acquisition of LWD data to 750 mbsf, however, provided Expedition 375 with key operational flexibility when returning to the site for coring. Because the turn-around time for shore-based processing of LWD data was typically ~3 days and this site was drilled close to the end of the expedition, our shipboard interpretations for this site are based on some unprocessed LWD data. The LWD logs at Site U1520 reveal numerous changes in physical properties downhole that match boundaries in the depth-converted seismic reflection data (Figure F12). As at the other sites, we found that changes in borehole conditions revealed by the ultrasonic caliper and other logging properties such as density, resistivity, porosity, and gamma ray coincide with changes in seismic reflection amplitudes and packages of seismic stratigraphy. In the upper and middle reaches of the borehole, we drilled through sequences we infer to be predominantly turbidites and the distal reaches of the Ruatoria MTD. Cores acquired during Expedition 375 confirmed that LWD data were acquired beneath the base of the Hikurangi Trough clastic sequence and into the inferred pelagic cover sequence of the Hikurangi Plateau.

### Observatory installations

Both of the complex, nested observatory installations were completed successfully. Each of the installations required a carefully coordinated sequence of operations, including several reentries, running and releasing multiple nested casing strings in deep water, and rigging large instrument strings, lengthy rope, and several hundred meters of hydraulic umbilical (see **Operations** in the Site U1518 chapter and **Operations** in the Site U1519 chapter [Saffer et al., 2019; Barnes et al., 2019b]). At Site U1518, the observatory included monitoring fluid pressure at three separate intervals and fluid sampling in the interior of the casing through a complex hole-completion design (Figure F4). At Site U1519, the observatory design was somewhat simpler but also included multiple nested casing strings and installation of an instrument string. We attribute the overall success of both observatory installations to a combination of

extensive pre-expedition preparation and to a carefully planned operations strategy for casing installation and instrument handling at the rig floor and moonpool. The design phase of the observatories began in collaboration with Texas A&M University (USA) engineering staff in April 2015 (~35 months in advance of Expedition 375). This preparation time was enabled by funding of the observatory development well in advance of the expedition and was essential to design and fabricate the observatory systems and to develop the implementation strategy.

Observatory operations generally went smoothly and, in some cases, more quickly than anticipated (e.g., running casing while strapping umbilical took less time than allotted in initial time estimates). However, a few minor problems were encountered during deployment that may compromise the observatory integrity at each site. At Site U1518, unexpected heave during reentry in the pre-drilled hole (U1518G) caused the drill pipe to bump and displace the reentry cone. As a result, we had no viable option other than to drill-in the ACORK system to its total depth of 423 mbsf at a new location (Hole U1518H) a few meters away from the previously drilled hole. Although it was fortunate that we were prepared to drill with a mud motor and underreamer, the proximity of a large open hole very near to the observatory installation raises two possibilities: (1) an extended time period may be required for the environment around the observatory borehole to reach thermal and chemical equilibrium and (2) hydraulic isolation from the seafloor may be compromised. However, we anticipate that this deep, large-diameter open hole will have collapsed soon after abandonment; initial download of the pressure data from the observatory will allow us to assess this. Because the casing string was drilled-in rather than lowered into a predrilled hole, it is also possible that the umbilical was damaged during installation and/or that the casing screens were fouled by circulation of a large volume of cuttings during drilling of the large-diameter hole. An additional potential issue at Site U1518 arose because the ROV platform (deployed by free-fall) hung up on the top of the ACORK wellhead. For this reason, we elected not to install an ROV platform at Site U1519.

At Site U1519, postinstallation inspection of the ACORK and CORK-II wellheads by the subsea camera revealed that the reentry funnel had filled with cuttings that partly bury the ACORK bays and the lower portion of the pressure sensor package. Potential future replacement of the sensor package, which is designed to be modular, will require removal of the cuttings before the sensor package can be replaced. The inspection also revealed that one of the support fins on the CORK-II wellhead was slightly damaged, likely during release using the J-tool. In general, these issues were unavoidable. However, based on these experiences, modification of installation operations may warrant consideration, for example, (1) to minimize the risk of large cuttings loads filling the ACORK reentry funnel, (2) to more reliably release wellheads without requiring drill string rotation (e.g., by using a hydraulic release as was used for the ACORK), and (3) to redesign the ACORK wellhead profile to minimize risk of ROV platform or other free-fall components becoming misaligned.

### Coring and sampling

At all of our coring sites (U1518–U1520 and U1526), the primary drilling and sampling objectives were met. At Site U1518, the formation was highly overconsolidated at the seafloor, and as a result we were unable to drill with the APC/XCB systems as deeply as planned and switched to RCB coring at a relatively shallow depth (<200 mbsf) to drill across the thrust fault. At Site U1520 (Hole

U1520C), we used a drill-in reentry system to case the upper portion of the sediment section; this system worked as planned and allowed us to reach our depth target in the volcanoclastic sequence. The original planned depth of the hole was 1200 mbsf, but the total depth was shallower because we had reached our main scientific objective. At Site U1526, we initially elected to undertake RCB coring in Hole U1526A because the primary target was the volcanoclastic and basaltic sequences of the seamount. However, sufficient time became available after completing operations at Site U1520 (near the end of the expedition) that we were able to return to Site U1526 to obtain a nearly complete section of the sedimentary sequence overlying the seamount in Hole U1526B with APC coring. At Site U1519, a highly targeted coring strategy was undertaken to maximize our efficiency with limited time. Here, we opted to spot core with the RCB system to collect material only from depths corresponding to the screened intervals of the observatory and in the lower part of the section where wellbore failures (breakouts) were observed in LWD data. Two more APC/HLAPC holes targeted shallow temperature and fluid chemistry measurements at Site U1519. This targeted approach yielded the key data needed to meet expedition science objectives.

The suite of cores obtained at Sites U1520 and U1526 reveal a surprising diversity of lithologies entering the subduction zone, including clastic trench fill material, carbonate-rich pelagic sediments, and a thick volcanoclastic sequence. Post-expedition research focused on the composition, diagenetic state, and physical properties of these lithologies will reveal the role that they play in SSE occurrence. Of particular interest are the extensive volcanoclastic deposits found in the lower portions of Sites U1520 and U1526; the alteration and diagenetic products of these materials may strongly influence the frictional properties and fluid content in the SSE source region. Correlating the lithologic sequences from Sites U1520 and U1526 into regional seismic data will provide important insight into the dominant lithologies in the SSE source region and their along-strike variations. Changes in pore water geochemistry observed throughout the Site U1520 section suggest evidence for recent fluid flow in lithologies recovered from the lower half. Fluid geochemistry also shows changes due to rapid sedimentation events in the upper, clastic portion of Site U1520.

At Site U1518, coring across an active shallow thrust fault provided new insights into the fault architecture, small-scale structural features, physical properties, and pore fluid geochemistry of an active fault that may be involved in SSEs. Post-expedition investigations will illuminate the hydrological and mechanical behavior of this active fault, particularly investigations related to fault structure and microstructures; analysis of pore fluid geochemistry variations across the fault; and laboratory studies of fault and wall rock friction, strength, and hydrological properties. These studies will also strongly complement the insights gained from the observatory samples and data (see above).

Drilling at Site U1519 aimed to characterize the upper plate physical and mechanical properties and thermal state. The approach of targeted spot coring was successful in obtaining samples needed to robustly interpret observatory pressure and temperature data and to extract quantitative information about in situ stress state from wellbore breakouts deeper than ~590 mbsf. Temperature measurements in the APC hole were also successful and provide valuable constraints for models that will define the thermal structure of the subduction zone and the temperature regime of the SSE source region.

Although the Expedition 375 priorities were focused on slow slip at subduction zones, we also recovered material that will give new insights into a range of other processes. Tephra layers, sometimes as thick as 1.5 m, were encountered throughout Sites U1518–U1520. These layers provide a nearly complete and continuous record of volcanic events at the Hikurangi subduction zone since the inception of subduction at the Hikurangi–Kermadec–Tonga Trench. Post-expedition research on the tephra will reveal changes in the magnitude, frequency, and source of arc volcanism. Pre-expedition interpretation of seismic reflection images suggested that Site U1520 would intersect the distal portions of the ~3150 km<sup>3</sup> Ruatoria debris avalanche deposit (Collot et al., 2001). However, evidence of mass transport processes in cores recovered from this unit is equivocal; further investigation is needed to determine if Site U1520 did indeed intersect the Ruatoria debris avalanche deposit. If so, the cores may provide important insights into processes associated with the emplacement of this massive debris avalanche deposit. Dating of basaltic material and detailed biostratigraphic and sedimentological investigation of sedimentary sequences recovered from Site U1526 will yield improved constraints on Hikurangi Plateau development, including its vertical tectonic history.

## References

- Araki, E., Saffer, D.M., Kopf, A.J., Wallace, L.M., Kimura, T., Machida, Y., Ide, S., Davis, E., and IODP Expedition 365 Shipboard Scientists, 2017. Recurring and triggered slow-slip events near the trench at the Nankai Trough subduction megathrust. *Science*, 356(6343):1157–1160. <https://doi.org/10.1126/science.aan3120>
- Audet, P., Bostock, M.G., Christensen, N.I., and Peacock, S.M., 2009. Seismic evidence for overpressured subducted oceanic crust and megathrust fault sealing. *Nature*, 457(7225):76–78. <https://doi.org/10.1038/nature07650>
- Baker, E.T., Lavelle, J.W., Feely, R.A., Massoth, G.J., Walker, S.L., and Lupton, J.E., 1989. Episodic venting of hydrothermal fluids from the Juan de Fuca Ridge. *Journal of Geophysical Research: Solid Earth*, 94(B7):9237–9250. <https://doi.org/10.1029/JB094iB07p09237>
- Barker, D.H.N., Henrys, S., Caratori Tontini, F., Barnes, P.M., Bassett, D., Todd, E., and Wallace, L., 2018. Geophysical constraints on the relationship between seamount subduction, slow slip and tremor at the north Hikurangi subduction zone, New Zealand. *Geophysical Research Letters*, 45(23):12804–12813. <https://doi.org/10.1029/2018GL080259>
- Barker, D.H.N., Sutherland, R., Henrys, S., and Bannister, S., 2009. Geometry of the Hikurangi subduction thrust and upper plate, North Island, New Zealand. *Geochemistry, Geophysics, Geosystems*, 10(2):Q02007. <https://doi.org/10.1029/2008GC002153>
- Barnes, P.M., Ghisetti, F.C., Ellis, S., and Morgan, J.K., 2018. The role of protothrusts in frontal accretion and accommodation of plate convergence, Hikurangi subduction margin, New Zealand. *Geosphere*, 14(2):440–468. <https://doi.org/10.1130/GES01552.1>
- Barnes, P.M., Lamarche, G., Bialas, J., Henrys, S., Pecher, I., Netzband, G.L., Greinert, J., Mountjoy, J.J., Pedley, K., and Crutchley, G., 2010. Tectonic and geological framework for gas hydrates and cold seeps on the Hikurangi subduction margin, New Zealand. *Marine Geology*, 272(1–4):26–48. <https://doi.org/10.1016/j.margeo.2009.03.012>
- Barnes, P.M., Pecher, I.A., LeVay, L.J., Bourlange, S.M., Brunet, M.M.Y., Cardona, S., Clennell, M.B., Cook, A.E., Crundwell, M.P., Dugan, B., Elger, J., Gamboa, D., Georgiopoulou, A., Greve, A., Han, S., Heesch, K.U., Hu, G., Kim, G.Y., Kitajima, H., Koge, H., Li, X., Machado, K.S., McNamara, D.D., Moore, G.F., Mountjoy, J.J., Nole, M.A., Owari, S., Paganoni, M., Petronotis, K.E., Rose, P.S., Scream, E.J., Shankar, U., Shepherd, C.L., Torres, M.E., Underwood, M.B., Wang, X., Woodhouse, A.D., and Wu, H.-Y., 2019a. Site U1517. In Pecher, I.A., Barnes, P.M., LeVay, L.J., and the Expedition 372A Scientists, *Creeping Gas Hydrate Slides*. Proceedings of the International Ocean Discovery Program, 372A: College Station, TX (International Ocean Discovery Program). <https://doi.org/10.14379/iodp.proc.372A.103.2019>
- Barnes, P.M., Wallace, L.M., Saffer, D.M., Pecher, I.A., Petronotis, K.E., LeVay, L.J., Bell, R.E., Crundwell, M.P., Engelmann de Oliveira, C.H., Fagereng, A., Fulton, P.M., Greve, A., Harris, R.N., Hashimoto, Y., Hüpers, A., Ikari, M.J., Ito, Y., Kitajima, H., Kutterolf, S., Lee, H., Li, X., Luo, M., Malie, P.R., Meneghini, F., Morgan, J.K., Noda, A., Rabinowitz, H.S., Savage, H.M., Shepherd, C.L., Shreedharan, S., Solomon, E.A., Underwood, M.B., Wang, M., Woodhouse, A.D., Bourlange, S.M., Brunet, M.M.Y., Cardona, S., Clennell, M.B., Cook, A.E., Dugan, B., Elger, J., Gamboa, D., Georgiopoulou, A., Han, S., Heesch, K.U., Hu, G., Kim, G.Y., Koge, H., Machado, K.S., McNamara, D.D., Moore, G.F., Mountjoy, J.J., Nole, M.A., Owari, S., Paganoni, M., Rose, P.S., Scream, E.J., Shankar, U., Torres, M.E., Wang, X., and Wu, H.-Y., 2019b. Site U1519. In Wallace, L.M., Saffer, D.M., Barnes, P.M., Pecher, I.A., Petronotis, K.E., LeVay, L.J., and the Expedition 372/375 Scientists, *Hikurangi Subduction Margin Coring, Logging, and Observatories*. Proceedings of the International Ocean Discovery Program, 372B/375: College Station, TX (International Ocean Discovery Program). <https://doi.org/10.14379/iodp.proc.372B375.104.2019>
- Barnes, P.M., Wallace, L.M., Saffer, D.M., Pecher, I.A., Petronotis, K.E., LeVay, L.J., Bell, R.E., Crundwell, M.P., Engelmann de Oliveira, C.H., Fagereng, A., Fulton, P.M., Greve, A., Harris, R.N., Hashimoto, Y., Hüpers, A., Ikari, M.J., Ito, Y., Kitajima, H., Kutterolf, S., Lee, H., Li, X., Luo, M., Malie, P.R., Meneghini, F., Morgan, J.K., Noda, A., Rabinowitz, H.S., Savage, H.M., Shepherd, C.L., Shreedharan, S., Solomon, E.A., Underwood, M.B., Wang, M., Woodhouse, A.D., Bourlange, S.M., Brunet, M.M.Y., Cardona, S., Clennell, M.B., Cook, A.E., Dugan, B., Elger, J., Gamboa, D., Georgiopoulou, A., Han, S., Heesch, K.U., Hu, G., Kim, G.Y., Koge, H., Machado, K.S., McNamara, D.D., Moore, G.F., Mountjoy, J.J., Nole, M.A., Owari, S., Paganoni, M., Rose, P.S., Scream, E.J., Shankar, U., Torres, M.E., Wang, X., and Wu, H.-Y., 2019c. Site U1520. In Wallace, L.M., Saffer, D.M., Barnes, P.M., Pecher, I.A., Petronotis, K.E., LeVay, L.J., and the Expedition 372/375 Scientists, *Hikurangi Subduction Margin Coring, Logging, and Observatories*. Proceedings of the International Ocean Discovery Program, 372B/375: College Station, TX (International Ocean Discovery Program). <https://doi.org/10.14379/iodp.proc.372B375.105.2019>
- Bell, R., Holden, C., Power, W., Wang, X., and Downes, G., 2014. Hikurangi margin tsunami earthquake generated by slow seismic rupture over a subducted seamount. *Earth and Planetary Science Letters*, 397:1–9. <https://doi.org/10.1016/j.epsl.2014.04.005>
- Bell, R., Sutherland, R., Barker, D.H.N., Henrys, S., Bannister, S., Wallace, L., and Beavan, J., 2010. Seismic reflection character of the Hikurangi subduction interface, New Zealand, in the region of repeated Gisborne slow slip events. *Geophysical Journal International*, 180(1):34–48. <https://doi.org/10.1111/j.1365-246X.2009.04401.x>
- Byrne, T.B., Lin, W., Tsutsumi, A., Yamamoto, Y., Lewis, J.C., Kanagawa, K., Kitamura, Y., Yamaguchi, A., and Kimura, G., 2009. Anelastic strain recovery reveals extension across SW Japan subduction zone. *Geophysical Research Letters*, 36(23):L23310. <https://doi.org/10.1029/2009GL040749>
- Chang, C., McNeill, L.C., Moore, J.C., Lin, W., Conin, M., and Yamada, Y., 2010. In situ stress state in the Nankai accretionary wedge estimated from borehole wall failures. *Geochemistry, Geophysics, Geosystems*, 11:Q0AD04. <https://doi.org/10.1029/2010GC003261>
- Collot, J.-Y., Lewis, K., Lamarache, G., and Lallemand, S., 2001. The giant Ruatoria debris avalanche on the northern Hikurangi margin, New Zealand; result of oblique seamount subduction. *Journal of Geophysical Research: Solid Earth*, 106(B9):19271–19297. <https://doi.org/10.1029/2001JB900004>
- Davis, E., Becker, K., Wang, K., and Kinoshita, M., 2009. Co-seismic and post-seismic pore-fluid pressure changes in the Philippine Sea plate and Nankai decollement in response to a seismogenic strain event off Kii Peninsula, Japan. *Earth, Planets Space*, 61(6):649–657. <https://doi.org/10.1186/BF03353174>



- Davis, E., Heesemann, M., and Wang, K., 2011. Evidence for episodic aseismic slip across the subduction seismogenic zone off Costa Rica: CORK borehole pressure observations at the subduction prism toe. *Earth and Planetary Science Letters*, 306(3–4):299–305. <https://doi.org/10.1016/j.epsl.2011.04.017>
- Davy, B., Hoernle, K., and Werner, R., 2008. Hikurangi Plateau: crustal structure, rifted formation, and Gondwana subduction history. *Geochemistry, Geophysics, Geosystems*, 9(7):Q07004. <https://doi.org/10.1029/2007GC001855>
- Expedition 319 Scientists, 2010. Methods. In Saffer, D., McNeill, L., Byrne, T., Araki, E., Toczko, S., Eguchi, N., Takahashi, K., and the Expedition 319 Scientists, *Proceedings of the Integrated Ocean Drilling Program*, 319: Tokyo (Integrated Ocean Drilling Program Management International, Inc.). <https://doi.org/10.2204/iodp.proc.319.102.2010>
- Fisher, A.T., and Wheat, C.G., 2010. Seamounts as conduits for massive fluid, heat, and solute fluxes on ridge flanks. *Oceanography*, 23(1):74–87. <https://doi.org/10.5670/oceanog.2010.63>
- Ghissetti, F.C., Barnes, P.M., Ellis, S., Plaza-Faverola, A.A., and Barker, D.H.N., 2016. The last 2 Myr of accretionary wedge construction in the central Hikurangi margin (North Island, New Zealand): insights from structural modeling. *Geochemistry, Geophysics, Geosystems*, 17(7):2661–2686. <https://doi.org/10.1002/2016GC006341>
- Hammerschmidt, S., Davis, E.E., and Kopf, A., 2013. Fluid pressure and temperature transients detected at the Nankai Trough megasplay fault: results from the SmartPlug borehole observatory. *Tectonophysics*, 600:116–133. <https://doi.org/10.1016/j.tecto.2013.02.010>
- Harris, R., Wallace, L., Webb, S., Ito, Y., Mochizuki, K., Ichihara, H., Henrys, S., et al., 2016. Investigations of shallow slow slip offshore of New Zealand. *Eos*, 9. <https://doi.org/10.1029/2016EO048945>
- Hensen, C., Wallmann, K., Schmidt, M., Ranero, C.R., and Suess, E., 2004. Fluid expulsion related to mud extrusion off Costa Rica—a window to the subducting slab. *Geology*, 32(3):201–204. <https://doi.org/10.1130/G20119.1>
- Huffman, K.A., and Saffer, D.M., 2016. In situ stress magnitudes at the toe of the Nankai Trough Accretionary Prism, offshore Shikoku Island, Japan. *Journal of Geophysical Research: Solid Earth*, 121(2):1202–1217. <https://doi.org/10.1002/2015JB012415>
- Jannasch, H.W., Wheat, C.G., Plant, J.N., Kastner, M., and Stakes, D.S., 2004. Continuous chemical monitoring with osmotically pumped water samplers: OsmoSampler design and applications. *Limnology and Oceanography: Methods*, 2(2):102–113. <https://doi.org/10.4319/lom.2004.2.102>
- Kastner, M., Solomon, E.A., Harris, R.N., and Torres, M.E., 2014. Fluid origins, thermal regimes, and fluid and solute fluxes in the forearc of subduction zones. In Stein, R., Blackman, D., Inagaki, F., and Larsen, H.-C., *Developments in Marine Geology (Volume 7): Earth and Life Processes Discovered from Subseafloor Environments: a Decade of Science Achieved by the Integrated Ocean Drilling Program (IODP)*. R. Stein (Series Ed.): Amsterdam (Elsevier B.V.), 671–733. <https://doi.org/10.1016/B978-0-444-62617-2.00022-0>
- Kinoshita, C., Saffer, D., Kopf, A., Roesner, A., Wallace, L.M., Araki, E., Kimura, T., et al., 2018. Changes in physical properties of the Nankai Trough Megasplay Fault induced by earthquakes, detected by continuous pressure monitoring. *Journal of Geophysical Research: Solid Earth*, 123(2):1072–1088. <https://doi.org/10.1002/2017JB014924>
- Kodaira, S., Iidaka, T., Kato, A., Park, J.-O., Iwasaki, T., and Kaneda, Y., 2004. High pore fluid pressure may cause silent slip in the Nankai Trough. *Science*, 304(5675):1295–1298. <https://doi.org/10.1126/science.1096535>
- Kopf, A., Mora, G., Deyhle, A., Frape, S., and Hesse, R., 2003. Fluid geochemistry in the Japan Trench forearc (ODP Leg 186): a synthesis. In Suyehiro, K., Sacks, I.S., Acton, G.D., and Oda, M. (Eds.), *Proceedings of the Ocean Drilling Program, Scientific Results*, 186: College Station, TX (Ocean Drilling Program), 1–23. <https://doi.org/10.2973/odp.proc.sr.186.117.2003>
- Leeman, J.R., Saffer, D.M., Scuderi, M.M., and Marone, C., 2016. Laboratory observations of slow earthquakes and the spectrum of tectonic fault slip modes. *Nature Communications*, 7:11104. <https://doi.org/10.1038/ncomms11104>
- Lewis, K.B., Collot, J.-Y., and Lallemand, S.E., 1998. The dammed Hikurangi Trough: a channel-fed trench blocked by subducting seamounts and their wake avalanches (New Zealand–France GeodyNZ Project). *Basin Research*, 10(4):441–468. <https://doi.org/10.1046/j.1365-2117.1998.00080.x>
- Lin, W., Conin, M., Moore, J.C., Chester, F.M., Nakamura, Y., Mori, J.J., Anderson, L., Brodsky, E.E., Eguchi, N., and Expedition 343 Scientists, 2013. Stress state in the largest displacement area of the 2011 Tohoku–Oki Earthquake. *Science*, 339(6120):687–690. <https://doi.org/10.1126/science.1229379>
- Liu, Y., and Rice, J.R., 2007. Spontaneous and triggered aseismic deformation transients in a subduction fault model. *Journal of Geophysical Research: Solid Earth*, 112(B9):B09404. <https://doi.org/10.1029/2007JB004930>
- Moos, D., and Zoback, M.D., 1990. Utilization of observations of well bore failure to constrain the orientation and magnitude of crustal stresses: application to continental, Deep Sea Drilling Project, and Ocean Drilling Program boreholes. *Journal of Geophysical Research: Solid Earth*, 95(B6):9305–9325. <https://doi.org/10.1029/JB095iB06p09305>
- Peacock, S.M., 2009. Thermal and metamorphic environment of subduction zone episodic tremor and slip. *Journal of Geophysical Research: Solid Earth*, 114(B8):B00A07. <https://doi.org/10.1029/2008JB005978>
- Pedley, K.L., Barnes, P.M., Pettinga, J.R., and Lewis, K.B., 2010. Seafloor structural geomorphic evolution of the accretionary frontal wedge in response to seamount subduction, Poverty Indentation, New Zealand. *Marine Geology*, 270(1–4):119–138. <https://doi.org/10.1016/j.margeo.2009.11.006>
- Peng, Z., and Gomberg, J., 2010. An integrated perspective of the continuum between earthquakes and slow-slip phenomena. *Nature Geoscience*, 3(9):599–607. <https://doi.org/10.1038/ngeo940>
- Plaza-Faverola, A., Klaeschen, D., Barnes, P., Pecher, I., Henrys, S., and Mountjoy, J., 2012. Evolution of fluid expulsion and concentrated hydrate zones across the southern Hikurangi subduction margin, New Zealand: an analysis from depth migrated seismic data. *Geochemistry, Geophysics, Geosystems*, 13(8):Q08019. <https://doi.org/10.1029/2012GC004228>
- Ranero, C.R., Grevemeyer, I., Sahling, U., Barckhausen, U., Hensen, C., Wallmann, K., Weinrebe, W., Vannucchi, P., von Huene, R., and McIntosh, K., 2008. Hydrogeological system of erosional convergent margins and its influence on tectonics and interplate seismogenesis. *Geochemistry, Geophysics, Geosystems*, 9(3):Q03S04. <https://doi.org/10.1029/2007GC001679>
- Rubinstein, J.L., Shelly, D.R., and Ellsworth, W.L., 2010. Non-volcanic tremor: a window into the roots of fault zones. In Cloetingh, S., and Negendank, J. (Eds.), *New Frontiers in Integrated Solid Earth Sciences*: Dordrecht, The Netherlands (Springer), 287–314. [https://doi.org/10.1007/978-90-481-2737-5\\_8](https://doi.org/10.1007/978-90-481-2737-5_8)
- Saffer, D., Wallace, L., and Petronotis, K., 2017. *Expedition 375 Scientific Prospectus: Hikurangi Subduction Margin Coring and Observatories*. International Ocean Discovery Program. <https://doi.org/10.14379/iodp.sp.375.2017>
- Saffer, D.M., Flemings, P.B., Boutt, D., Doan, M.-L., Ito, T., McNeill, L., Byrne, T., et al., 2013. In situ stress and pore pressure in the Kumano Forearc Basin, offshore SW Honshu from downhole measurements during riser drilling. *Geochemistry, Geophysics, Geosystems*, 14(5):1454–1470. <https://doi.org/10.1002/ggge.20051>
- Saffer, D.M., Underwood, M.B., and McKiernan, A.W., 2008. Evaluation of factors controlling smectite transformation and fluid production in subduction zones: application to the Nankai Trough. *Island Arc*, 17(2):208–230. <https://doi.org/10.1111/j.1440-1738.2008.00614.x>
- Saffer, D.M., and Wallace, L.M., 2015. The frictional, hydrologic, metamorphic and thermal habitat of shallow slow earthquakes. *Nature Geoscience*, 8(8):594–600. <https://doi.org/10.1038/ngeo2490>
- Saffer, D.M., Wallace, L.M., Barnes, P.M., Pecher, I.A., Petronotis, K.E., LeVay, L.J., Bell, R.E., Crundwell, M.P., Engelmann de Oliveira, C.H., Fagereng, A., Fulton, P.M., Greve, A., Harris, R.N., Hashimoto, Y., Hüpers, A., Ikari, M.J., Ito, Y., Kitajima, H., Kutterolf, S., Lee, H., Li, X., Luo, M., Malie, P.R., Meneghini, F., Morgan, J.K., Noda, A., Rabinowitz, H.S., Savage, H.M., Shepherd, C.L., Shreedharan, S., Solomon, E.A., Underwood, M.B.,

- Wang, M., Woodhouse, A.D., Bourlange, S.M., Brunet, M.M.Y., Cardona, S., Clennell, M.B., Cook, A.E., Dugan, B., Elger, J., Gamboa, D., Georgiopolou, A., Han, S., Heeschen, K.U., Hu, G., Kim, G.Y., Koge, H., Machado, K.S., McNamara, D.D., Moore, G.F., Mountjoy, J.J., Nole, M.A., Owari, S., Paganoni, M., Rose, P.S., Sreaton, E.J., Shankar, U., Torres, M.E., Wang, X., and Wu, H.-Y., 2019. Site U1518. In Wallace, L.M., Saffer, D.M., Barnes, P.M., Pecher, I.A., Petronotis, K.E., LeVay, L.J., and the Expedition 372/375 Scientists, *Hikurangi Subduction Margin Coring, Logging, and Observatories*. Proceedings of the International Ocean Discovery Program, 372B/375: College Station, TX (International Ocean Discovery Program).  
<https://doi.org/10.14379/iodp.proc.372B375.103.2019>
- Sawyer, A.H., Flemings, P., Elsworth, D., and Kinoshita, M., 2008. Response of submarine hydrologic monitoring instruments to formation pressure changes: theory and application to Nankai advanced CORKs. *Journal of Geophysical Research: Solid Earth*, 113(B1):B01102.  
<https://doi.org/10.1029/2007JB005132>
- Schwartz, S.Y., and Rokosky, J.M., 2007. Slow slip events and seismic tremor at circum-Pacific subduction zones. *Reviews of Geophysics*, 45(3):RG3004.  
<https://doi.org/10.1029/2006RG000208>
- Solomon, E.A., and Kastner, M., 2012. Progressive barite dissolution in the Costa Rica forearc—implications for global fluxes of Ba to the volcanic arc and mantle. *Geochimica et Cosmochimica Acta*, 83:110–124.  
<https://doi.org/10.1016/j.gca.2011.12.021>
- Solomon, E.A., Kastner, M., Wheat, C.G., Jannasch, H., Robertson, G., Davis, E.E., and Morris, J.D., 2009. Long-term hydrogeochemical records in the oceanic basement and forearc prism at the Costa Rica subduction zone. *Earth and Planetary Science Letters*, 282(1–4):240–251.  
<https://doi.org/10.1016/j.epsl.2009.03.022>
- Song, T.-R.A., Helmlberger, D.V., Brudzinski, M.R., Clayton, R.W., Davis, P., Pérez-Campos, X., and Singh, S.K., 2009. Subducting slab ultra-slow velocity layer coincident with silent earthquakes in southern Mexico. *Science*, 324(5926):502–506. <https://doi.org/10.1126/science.1167595>
- Tobin, H.J., and Saffer, D.M., 2009. Elevated fluid pressure and extreme mechanical weakness of a plate boundary thrust, Nankai Trough subduction zone. *Geology*, 37(8):679–682.  
<https://doi.org/10.1130/G25752A.1>
- Vannucchi, P., Ujiie, K., Stronck, N., and the IODP Expedition 334 Science Party, 2013. IODP Expedition 334: an investigation of the sedimentary record, fluid flow and state of stress on top of the seismogenic zone of an erosive subduction margin. *Scientific Drilling*, 15:23–30.  
<https://doi.org/10.2204/iodp.sd.15.03.2013>
- Wallace, L.M., and Beavan, J., 2010. Diverse slow slip behavior at the Hikurangi subduction margin, New Zealand. *Journal of Geophysical Research: Solid Earth*, 115(B12):B12402. <https://doi.org/10.1029/2010JB007717>
- Wallace, L.M., Beavan, J., McCaffrey, R., and Darby, D., 2004. Subduction zone coupling and tectonic block rotations in the North Island, New Zealand. *Journal of Geophysical Research: Solid Earth*, 109(B12):B12406.  
<https://doi.org/10.1029/2004JB003241>
- Wallace, L.M., Kaneko, Y., Hreinsdóttir, S., Hamling, I., Peng, Z., Bartlow, N., D'Anastasio, E., and Fry, B., 2017. Large-scale dynamic triggering of shallow slow slip enhanced by overlying sedimentary wedge. *Nature Geoscience*, 10(10):765–770. <https://doi.org/10.1038/ngeo3021>
- Wallace, L.M., Saffer, D.M., Petronotis, K.E., Barnes, P.M., Bell, R.E., Crundwell, M.P., Engelmann de Oliveira, C.H., Fagereng, A., Fulton, P.M., Greve, A., Harris, R.N., Hashimoto, Y., Hüpers, A., Ikari, M.J., Ito, Y., Kitajima, H., Kutterolf, S., Lee, H., Li, X., Luo, M., Malie, P.R., Meneghini, F., Morgan, J.K., Noda, A., Rabinowitz, H.S., Savage, H.M., Shepherd, C.L., Shreedharan, S., Solomon, E.A., Underwood, M.B., Wang, M., and Woodhouse, A.D., 2019. Site U1526. In Wallace, L.M., Saffer, D.M., Barnes, P.M., Pecher, I.A., Petronotis, K.E., LeVay, L.J., and the Expedition 372/375 Scientists, *Hikurangi Subduction Margin Coring, Logging, and Observatories*. Proceedings of the International Ocean Discovery Program, 372B/375: College Station, TX (International Ocean Discovery Program).  
<https://doi.org/10.14379/iodp.proc.372B375.106.2019>
- Wallace, L.M., Webb, S.C., Ito, Y., Mochizuki, K., Hino, R., Henrys, S., Schwartz, S.Y., and Sheehan, A.F., 2016. Slow slip near the trench at the Hikurangi subduction zone, New Zealand. *Science*, 352(6286):701–704.  
<https://doi.org/10.1126/science.aaf2349>
- Wang, K., 2004. Applying fundamental principles and mathematical models to understand processes and estimate parameters. In Davis, E.E., and Elderfield, H. (Eds.), *Hydrogeology of the Oceanic Lithosphere*: Cambridge, United Kingdom (Cambridge University Press), 376–413.
- Wang, K., and Davis, E.E., 1996. Theory for the propagation of tidally induced pore pressure variations in layered seafloor formations. *Journal of Geophysical Research: Solid Earth*, 101(B5):11483–11495.  
<https://doi.org/10.1029/96JB00641>
- Wech, A.G., and Creager, K.C., 2011. A continuum of stress, strength and slip in the Cascadia subduction zone. *Nature Geoscience*, 4(9):624–628.  
<https://doi.org/10.1038/ngeo1215>
- Williams, C.A., and Wallace, L.M., 2018. The impact of realistic elastic properties on inversions of shallow subduction interface slow slip events using seafloor geodetic data. *Geophysical Research Letters*, 45(15):7462–7470.  
<https://doi.org/10.1029/2018GL078042>
- Zoback, M.D., Hickman, S., and Ellsworth, W., 2007. The role of fault zone drilling. In Kanamori, H., and Schubert, G. (Eds.), *Treatise on Geophysics* (Volume 4): *Earthquake Seismology*: Amsterdam (Elsevier), 649–674.  
<https://doi.org/10.1016/B978-044452748-6/00084-5>